Annual Technical Report – Year II

Covering the period of October 2, 2002 to October 1, 2003

Deliverable: Subcontract Article 3 B, **Item 13 (**ADJ-2-30630-13**)**

Project: Fundamental Materials Research and Advanced Process Development for Thin-Film CIS-Based Photovoltaics

P.I.:   T. J. Anderson

Co-PI's: Sheng S. Li , O. D. Crisalle, and R. K. Singh

Other Personnel: Valentin Craciun, Ryan Acher, Ozge Erdogdu, Joshua Howard, Chia-Hua Huang, Ryan Kaczynski, Lei Li Kerr, Woo Kyoung Kim, Matt Monroe, Seemant Rawal, Wei Liu, Jiyon Song, Xuege Wang, Seokhyun Yoon

Subcontract No.:   ADJ-2-30630-13

Funding Agency: National Renewal Energy Laboratory (NREL)

Program: Thin-Film Photovoltaics Partnership program

Contact Address: Tim Anderson, P.O. Box 116005, 227 Chemical Engineering Bldg., University of Florida, Gainesville FL 32611-6005, Phone: (352) 392-0882, FAX: (352) 392-9513, E-mail: tim@nersp.nerdc.ufl.edu

1   Investigation of Pulsed Non-melt Laser Annealing (NLA) of CIGS-Based Solar Cells

Participants: Sheng S. Li (Faculty Advisor), Xuege Wang, Lei Li Kerr, S. Rawal, J. M. Howard, V. Craciun, T. J. Anderson, O. D. Crisalle.

1.1 Objectives

The objective of this project is to study the effect of Non-melt Laser Annealing (NLA) on electrical and optical properties of the CIS/CIGS based solar cell, and to find the optimal laser condition in order to improve the cell's performance.

1.2 Accomplishments

Pulsed Non-melt Laser Annealing (NLA) has been used to modify the near surface defect density and related junction properties in CIGS solar cells. CIGS films deposited on Mo/glass substrates were annealed by the NLA technique at selected laser energy densities and pulse number, and characterized by the Dual Beam Optical Modulation (DBOM), XRD, SEM, and Hall measurements. In addition, selected annealed CIGS/CdS films processed by NLA were fabricated into cells, and characterized by the photo I-V and Q-E measurements. The results suggest that low power NLA treatment could enhance the effective carrier lifetime, mobility, film grain size, and sheet resistance and lower the near-surface defect density in the films. Since the results also show that the optimal energy density of NLA should be under $50mJ/cm^2$, an additional set of CIGS films deposited on Mo/glass substrates were annealed by the NLA technique at selected laser energy densities and pulse number, and fabricated into finished cells, and characterized by the photo I-V and Q-E measurements. The new results suggest that low power NLA treatment could improve the I-V performance of CIGS cells.

1.2.1   Preliminary characterization results of Non-Melt Laser Annealed CIGS films

Laser annealing of CIGS and CIGS/CdS samples was performed using a 248 nm line Kr Excimer laser, operated with a pulse width of 25 ns, and energy density in the range of 20 to 60 mJ/cm^2. The non-destructive Dual Beam Optical Modulation (DBOM) technique developed in Dr. Li's lab was used to measure the effective carrier lifetimes in the CIGS absorber [1, 2], and to evaluate the effect of NLA on the performance of CIGS cells. Within the sensitivity of the DBOM measurement, the effective carrier lifetimes were found to increase for CIGS films annealed with 5 pulses laser beam each having an energy density in the range of 30 to 60 mJ/cm^2. The results shown in Table 1-1 indicate that low power NLA treatments increase the effective lifetimes of the annealed samples. The relationship between the energy density of the laser beam and the increase of effective carrier lifetime is still unclear. Previous XRD analysis of CIGS and CIGS/CdS samples before and after laser annealing revealed sharper peaks attributable to the CIGS phases, consistent with increased crystallinity. SEM result shows that the surface morphology and apparent grain size changed upon laser annealing. These results suggest that the

energy density was sufficient to cause atomic rearrangement in the near surface region, and thus the potential for modifying the atomic defects in the region.

Table 1-1. Effective lifetimes of NLA CIGS samples.

Sample #	Carrier lifetime before NLA	Carrier lifetime after NLA	NLA condition
CIGS#1	1.77 ns	4.87 ns	30m J/cm^2, 5 pulses
CIGS#2	2.82 ns	3.39 ns	40m J/cm^2, 5 pulses
CIGS#3	4.1 ns	5.43 ns	50m J/cm^2, 5 pulses
CIGS#4	4.5 ns	6.31 ns	60m J/cm^2, 5 pulses

1.2.2   The Hall- effect measurements of NLA CIGS films

Based on the encouraging DBOM results from the initial NLA treatment of CIGS samples, a second set of experiments was performed in which the energy density and pulse number of the incident laser radiation were varied. Hall effect measurement was made on the CIGS samples prior and after annealing to determine the effect of NLA treatment on the carrier concentration, mobility, and resistivity of the CIGS films.

Four CIGS films deposited on the glass substrate were treated with pulsed NLA at room temperature. The annealing conditions and the results of Hall effect measurements are summarized in Table 1-2. These results show a significant increase in the value of Hall mobility and decrease in film resistivity after NLA treatment. The carrier mobilities of the NLA treated samples were found 3 to 4 times greater than the values before annealing. Although the hole density was found to decrease slightly with annealing, the film resistivity was decreased by 72% and 64% for the samples treated at an energy density of 20 mJ/cm^2 (samples 1H and 2H, respectively). At a higher energy density of 40 mJ/cm^2 the film resistivity was changed by more than 95% of the unannealed value (samples 3H and 4H). Thus, both the energy density and the number of pulse cycle of the laser beam could play an important role in determining the resistivity of CIGS absorber layers.

Table 1-2. Results of Hall effect measurements on laser annealed (NLA) CIGS samples.

Sample #	Before NLA			After NLA				
	Hole density (cm^{-3})	Hall mobility $(cm^2/V\text{-}s)$	Resistivity $(\Omega\text{-}cm)$	Energy Density (mJ/cm^2)	Pulse #	Hole density (cm^{-3})	Hall mobility $(cm^2/V\text{-}s)$	Resistivity $(\Omega\text{-}cm)$
#1H	$5.3*10^{15}$	8.89	133	20	10	$4.45*10^{15}$	37.6	37.3
#2H	$2.9*10^{16}$	0.93	235	20	20	$2.43*10^{16}$	2.977	86.4
#3H	$4.3*10^{16}$	1.54	94	40	10	$1.8*10^{16}$	6.1	2.67
#4H	$7.1*10^{16}$	0.60	148	40	20	$3.3*10^{16}$	2.8	4.64

1.2.3 The Photo- I-V measurements of NLA CIGS cells

Four CIGS/CdS samples were annealed by a 50 mJ/cm^2 laser beam with different pulse number. Two samples were followed by a 100 Å extra CdS buffer layer re-growth after NLA treatment on the CIGS samples initially coated with a 400 Å CBD CdS buffer layer, and one control sample without any treatment. These samples were then fabricated into cells for testing. The DBOM and photo- I-V results are summarized in Table 1-3, which show an increase in the effective carrier lifetimes on the NLA treated samples. No explicit improvements, however, were found in the photo- I-V results of the annealed cells. The data also show slight decreasing in the fill factor and conversion efficiency of cells annealed with 20 pulses NLA compared with the 10-pulse-annealed cells. Some high energy density (i.e., 80 mJ/cm^2) NLA treatments were also used on other CIGS samples, and the results show a drastic reduction in the cell efficiency. These results suggest that an optimal NLA energy density should be less than 50 mJ/cm^2, and no significant influence on the cell performance due to the additional CdS buffer layer re-growth was found in this study.

Table 1-3. Effective lifetimes and I-V results of NLA CIGS/CdS samples and devices.

Sample #	Lifetime(ns)	Vo (V)	Jsc(mA/cm^2)	F.F.(%)	Eff.%	NLA condition
CIGS/CdS #0	3.76	0.42	27.2	53.11	6.14	Control sample
CIGS/CdS #1	4.77	0.45	24.83	54.43	6.17	50mJ/cm^2, 10 pulses
CIGS/CdS #2	4.11	0.44	26.98	51.37	6.15	50mJ/cm^2, 20 pulses
CIGS/CdS #3	5.2	0.45	26.19	54.06	6.27	50mJ/cm^2, 10 pulses w/CdS re-growth
CIGS/CdS #4	3.86	0.39	26.43	44.25	4.57	50mJ/cm^2, 20 pulses w/CdS re-growth

1.2.4 Q-E measurements of NLA CIGS cells

Two CIGS films with a 500 Å CdS buffer layer were annealed at an energy density of 50 mJ/cm2, and then fabricated into cells. To study the effect of pulsed NLA treatment, the spectral response and quantum efficiency (Q-E) were measured on these cells. The results shown in Figures 1-1 and 1-2 indicate that for incident light with wavelengths greater than 650 nm, the Q-E and spectral response of the NLA cells are higher than those of the control cell, indicating that the NLA treatment increases the effective carrier lifetime and diffusion length in the absorber layer and hence increases the short-circuit current density in comparison to the control cell without NLA treatment. In the short wavelength regime ($\lambda < 0.65$ μm), however, the Q-E and spectral response decrease after NLA treatment, which suggest damages near the interface region of CIGS/CdS films by the laser beam. As a result, the surface recombination velocity is increased and the Q-E and spectral response are lower in the shorter wavelength region. It is also noted that the values of Q-E and spectral response for sample annealed with 20 cycles laser pulse were found to be lower than the sample with 10 cycles of annealing pulse with same energy density.
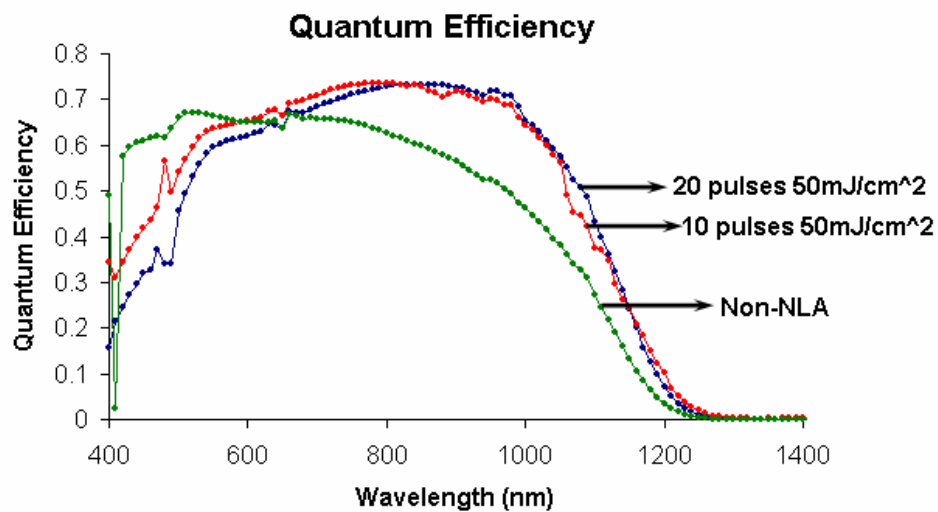
Figure 1-1. Quantum efficiency of CIGS cells with and without NLA treatment.
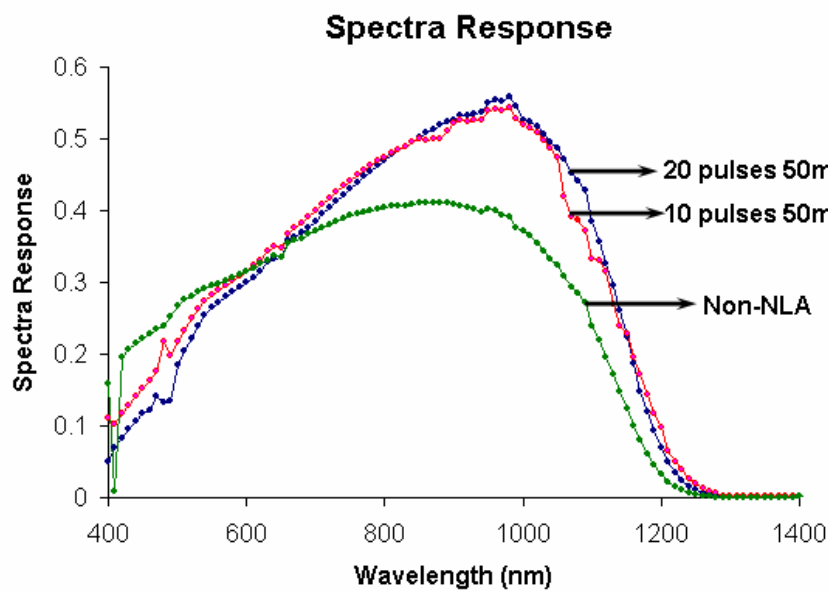

Figure 1-2. Spectral response of CIGS cells with and without NLA treatment.

1.2.5   Additional experiments under the optimized NLA condition

Since the previous results suggest that an optimal NLA energy density should be less than 50 mJ/cm^2, an additional set of CIGS/CdS samples treated by NLA with different energy densities (less than 50 mJ/cm^2) and pulse number were fabricated into finished devices. The NLA conditions and photo- I-V results of these samples are summarized in Table 1-4. At this time, explicit improvements were found in the photo- I-V results of the annealed cells under 30mJ/cm^2, 5 pulses and 10 pulses NLA conditions. The data also show decreasing in all I-V performance parameters of the cells annealed by laser beam with energy density higher than 30mJ/cm^2. These results suggest that an optimal NLA energy density should be around 30 mJ/cm^2, 5 pulses. Figure 1-3 shows the trend of I-V parameters versus NLA condition. A slight increase of cell performance was found with NLA condition of 30mJ/cm^2, 5 pulses compared to the 10 pulses NLA cells. In addition, the quantum efficiency (Q-E) was measured of the two cells annealed by laser beam with 30 mJ/cm^2 energy density and the control cell. Similarly, the new Q-E result shows the same trend with the previous experiment results (Figure 1-1).

Table 1-4. Photo- I-V results of NLA CIGS Solar cells.

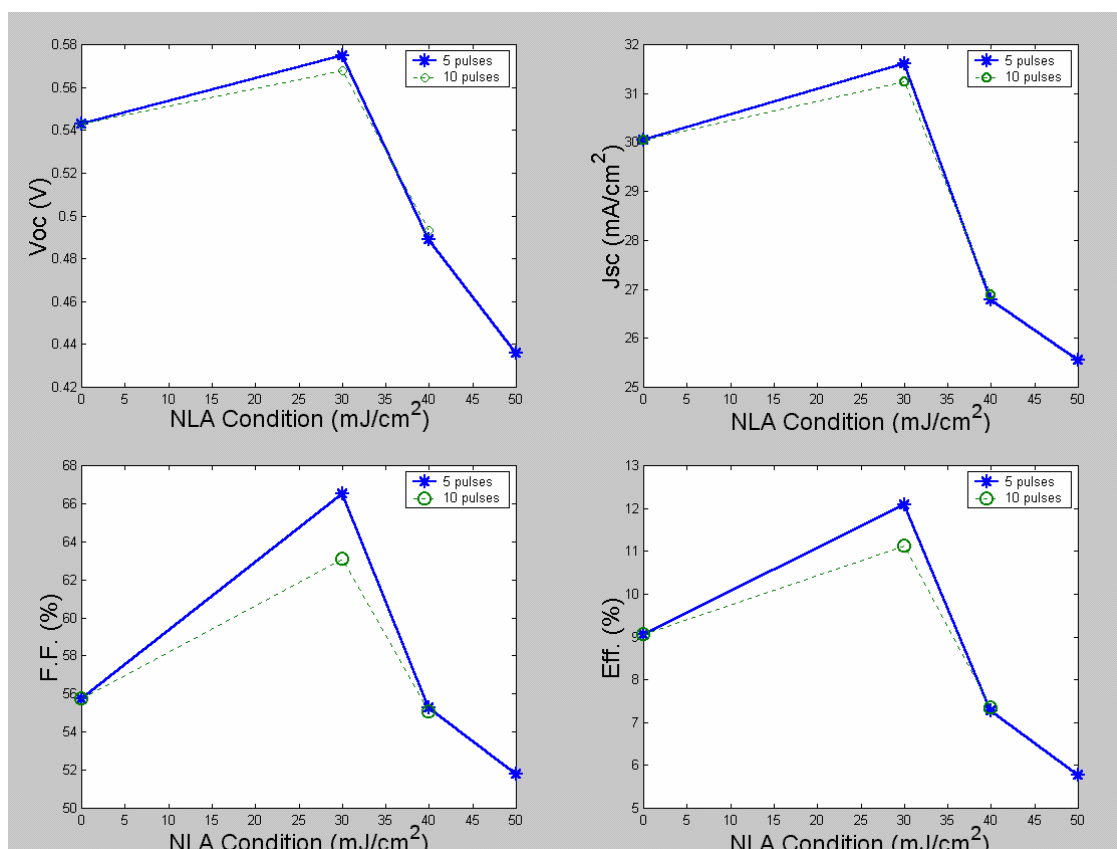| Sample #	Voc (V)	Jsc(mA/cm^2)	F.F.(%)	Eff.%	NLA condition
CIGS/CdS #1	0.576	31.6	66.50	12.074	30mJ/cm^2, 5 pulses
CIGS/CdS #2	0.568	31.25	63.11	11.12	30mJ/cm^2, 10 pulses
CIGS/CdS #3	0.489	26.79	55.29	7.268	40mJ/cm^2, 5 pulses
CIGS/CdS #4	0.493	26.89	55.08	7.34	40mJ/cm^2, 10 pulses
CIGS/CdS #5	0.436	25.56	51.8	5.773	50mJ/cm^2, 5 pulses
CIGS/CdS #6	0.543	30.05	55.74	9.064	Control sample

Figure 1-3.   Open-circuit voltage (Voc), short-circuit current (Jsc), fill factor (F.F.), and conversion efficiency (Eff.) versus different NLA conditions.

1.2.6 Conclusions

The effect of pulsed NLA treatment on the CIGS-based solar cells was investigated under selected annealing conditions. Several characterization techniques (DBOM, XRD, SEM, Hall-effect, I-V and Q-E measurements) support the conclusion that pulsed NLA treatment under an optimal laser energy density condition can significantly improve the effective carrier lifetime, carrier mobility, surface morphology, spectral response (Q.E.) [3] and hence the cell performance. The energy density of the laser beam and the number of pulse cycle play a key role in modifying the optical and electrical properties of the CIGS absorbers and hence the cell performance.

1.3   Publications and presentations

1.   Xuege Wang, Sheng S. Li, C. H. Huang, Lei Li Kerr, S. Rawal, J. M. Howard, V. Craciun, T. J. Anderson, O. D. Crisalle, and R. K. Singh. "Investigation of Pulsed Non-melt Laser Annealing (NLA) of CIGS-Based Solar Cells", published in the Conf. Proceedings of *the 3rd World Conference on Photovoltaic Energy Conversion* (WCPEC-3) (2003).

2. Xuege Wang, Sheng S. Li, C. H. Huang, Lei Li Kerr, S. Rawal, J. M. Howard, V. Craciun, T. J. Anderson, O. D. Crisalle, and R. K. Singh. "Investigation of Pulsed Non-melt Laser Annealing (NLA) of CIGS-Based Solar Cells", published in the Proceedings of *the 2003 NCPV and Solar Program Review Meeting* (2003).

3. Xuege Wang, Sheng S. Li, C. H. Huang, Lei Li Kerr, S. Rawal, J. M. Howard, V. Craciun, T. J. Anderson, O. D. Crisalle, and R. K. Singh. "Investigation of Pulsed Non-melt Laser Annealing (NLA) of CIGS-Based Solar Cells", presented in poster session in *the 3rd World Conference on Photovoltaic Energy Conversion* (WCPEC-3) (2003).

4. Xuege Wang, Sheng S. Li, C. H. Huang, Lei Li Kerr, S. Rawal, J. M. Howard, V. Craciun, T. J. Anderson, O. D. Crisalle, and R. K. Singh. "Investigation of Pulsed Non-melt Laser Annealing (NLA) of CIGS-Based Solar Cells", presented at *the 2003 NCPV Review Meeting,* Denver, March 24-26 (2003).

1.4 References cited

[1] Sheng S. Li, B.J. Stanbery, C.H. Huang, C.H. Chang, Y.S. Chang, and T.J. Anderson, "Effects of buffer layer processing on CIGS excess carrier lifetime: application of dual-beam optical modulation to process analysis [of solar cells]," conference record of 25th IEEE PVSC, pp. 821-824, 1996.

[2] C.H. Huang, Sheng S. Li, B.J. Stanbery, C.H. Chang, and T.J. Anderson, "Investigation of buffer layer process on CIGS solar cells by dual beam optical modulation technique," conference record of 26th IEEE PVSC, pp. 407-410, 1997.

[3] Xuege Wang, Sheng S. Li, C. H. Huang, Lei Li Kerr, S. Rawal, J. M. Howard, V. Craciun, T. J. Anderson, O. D. Crisalle, and R. K. Singh. "Investigation of Pulsed Non-melt Laser Annealing (NLA) of CIGS-Based Solar Cells", *the 3rd World Conference on Photovoltaic Energy Conversion* (WCPEC-3) (2003).

2 Investigation of Deep-Level Defects in Cu(In,Ga)Se₂ Solar Cells by Deep-Level Transient Spectroscopy

Participants: Sheng S. Li, Kerr, Lei Li, S. W. Johnston, J. Abushama, R. N. Noufi, Xuege Wang, T. J. Anderson, and O. D. Crisalle.

2.1 Objectives

The objective of this task is to investigate the deep-level defects in Cu(In,Ga)Se₂ solar cells by using the Deep-Level Transient Spectroscopy (DLTS) technique.

2.2 Accomplishments

The performance of the chalcopyrite material Cu(In,Ga)Se₂ used as an absorber layer in thin-film photovoltaic devices is significantly affected by the presence of native defects. Deep-level transient spectroscopy (DLTS) technique is used in this work to address the current lack of fundamental understanding of absorber-defect properties, yielding relevant information about the defect types, their capture cross-sections, and energy levels and densities. Three solar cells developed using different absorber growth technologies were analyzed using DLTS, capacitance-voltage (C-V), and capacitance-temperature (C-T) techniques. It was found that a cell produced at the University of Florida (UF) exhibits a middle-gap defect that may explain the cell's low fill factor and low open-circuit voltage values observed. A highly efficient cell produced by the National Renewable Energy Laboratory (NREL) was found to contain three minority carrier traps; however, high cell performance is nevertheless retained because these shallow-traps are not effective recombination centers. The approach followed using the DLTS technique serves as a paradigm for revealing the presence of significant defect levels in absorber materials, and may be used to support the identification of remedial processing operations.

2.2.1 Introduction

Chalcopyrite CuInSe₂ (CIS) and its alloy Cu(In,Ga)Se₂ in polycrystalline form holds great potential for photovoltaic applications. Unlike conventional binary semiconductors (such as GaAs or ZnSe), it can tolerate a large range of anion-to-cation off-stoichiometry, a convenience since Cu-deficient and/or In-deficient stoichiometries are stable and useful. This brings an advantage in terms of opportunities for band gap engineering and defect chemistry modifications. The large composition homogeneity range and the deviation from stoichiometry in compound semiconductors such as CIGS is often attributed to antisite defects, vacancies, and defect clusters in the material. It is known that CIS can be produced in both p- and n- type resistivity characteristics by introduction of *native* defects with or without extrinsic impurities. However, the doping mechanism and point defect chemistry of CIS are not well understood at the fundamental level. Therefore, it is important to advance the understanding of these properties to further improve the cell efficiency and reduce the cost of solar cells. Deep- level defects play an important role in determining the recombination and trapping mechanisms (and

hence the minority carrier lifetimes) in a semiconductor.

Zhang *et al.* [1] has calculated the transition energy for a large number of defects in CIS materials. However, there are some discrepancies between those calculations and the experimental observation [1]. According to the photoluminescence spectroscopy measurements by Schõn and Bucher [2], the In_{Cu} defect is a shallow donor with an ionization energy of E_c-0.2 eV (*i.e.*, 0.2 eV below the conduction band). In the calculations reported in Zhang *et al.* [1] the anion site defect was neglected. However, many other researchers believe that the selenium vacancy V_{Se} is the shallowest donor level, with an energy level of E_c-0.06 eV, and that it could lead to a significant lattice relaxation during the ionization process [3]. The energy levels and densities of deep-level defects are important input parameters for developing an accurate device model for CIS-based thin-film solar cells. The DLTS technique is a powerful tool for determining the defect properties such as trap energy level, capture cross section, and trap concentration in a semiconductor.

2.2.2 Experimental Procedure

The DLTS technique is used to measure the transient capacitance change in CIS–based solar cells after deep-level traps in the space charge region are filled with either the majority or minority carrier charges. More specifically, the density and energy level of these deep-level traps are determined from the DLTS and C-V measurements.

By scanning the capacitance change over a wide range of temperatures under different rate windows, the electron emission rate e_n as a function of inverse temperature T^{-1} can be obtained. The results are represented in the form of an Arrhenius plot, *i.e.*, ln $(T^2 ô)$ versus T^{-1}, where $ô = 1/e_n$, from which it is possible to extract the activation energy E_a and the capture cross-section σ_n. The electron emission-rate equation is given by

$$e_n = \sigma_n \ v_{th} \ N_c \ exp(-E_a / (kT)) \qquad (2\text{-}1)$$

where v_{th} is the thermal velocity and N_c is the effective density of conduction band states. The electron trap density, N_T, can be calculated by using

$$N_T, = 2 \ \Delta C \ N_a / C_0 \qquad (2\text{-}2)$$

where N_a is the net hole concentration; ΔC is the capacitance change due to the emission of charge carriers from the trap level, which is proportional to the probed trap concentration; and C_0 the zero-bias capacitance, which can be obtained from the capacitance *versus* temperature (C-T) scan at the corresponding DLTS peak temperature. Equation (2-2) is valid for the case when N_T is smaller than N_a. Finally, the net hole concentration N_a in a p-type CIGS absorber layer can be determined via the C-V or Hall effect measurements.

2.2.3   Results and Discussion

DLTS studies were conducted on three types of CIS and CIGS cells:

(i)   CIS cells (UF CIS cells) developed by the University of Florida using a bilayer precursor process.

(ii)   CIGS cells (EPV CIGS cells) fabricated by Energy Photovoltaics Inc., using physical-vapor deposition process.

(iii)   CIGS cells (NRELCIGS cells) fabricated by the National Renewable Energy Laboratory using a three-stage precursor process.

Details of the DLTS measurements and analyses are discussed as follows:

2.2.3.1   *Analysis of UF CIS cells*

(a) Background and material growth procedure

An alternative growth process for $CuInSe_2$ (CIS) films has been developed by the research team at the University of Florida (UF) in Gainesville, Florida.   In this approach, a binary two-layer precursor Cu-Se/In-Se film is first deposited on a Mo-coated glass substrate at low temperature using the migration enhanced epitaxy (MEE) technique (a variant of molecular-beam deposition) [5].   The films are then subjected to rapid thermal processing (RTP) under a carefully controlled Se ambient, leading to the synthesis of a single-phase $CuInSe_2$ film.   A schematic diagram of the two-layer precursor structure for growing α-$CuInSe_2$ is shown in Figure 2-1. It consists of a slightly Se-rich In-Se binary layer deposited at low temperature on a Mo-on-glass substrate, followed by the deposition of a Se-rich Cu-Se binary layer.   The binary layers are deposited at ~200˚C using the MEE process, and are subsequently annealed via RTP.

This composition of the binary structures was suggested by examination of the Cu-In-Se phase diagram for conditions that show α-CIS in equilibrium with a liquid phase at a low temperature.   Precursor layer compositions were then selected on the likelihood of forming the liquid phase while avoiding high melting temperature compounds.   Figure 2-2 illustrates the isothermal composition diagram of Cu-In-Se system at 500˚C [6].   The α- CIS phase is seen to lie on the tie line connecting the In_2Se_3 and Cu_2Se phases, and shows a solid solution range of several atomic-percentage values.   Note that a low-temperature single phase Se-rich liquid solution is located near the Se corner of the phase diagram.   The triangle connecting the α-CIS phase boundary to the Se corner represents the two-phase region consisting of α-CIS plus Se-rich liquid, which is the target for the overall film composition.   Phase diagram calculations suggest that the Se-rich liquid phase can exist at a temperature as low as 211˚C.   They also suggest that the synthesized CIS films will be Se-rich, and that excess Se can easily volatilize during annealing. Starting from the binary metal-Se layers in direct contact promises to avoid reactions that yield high melting temperature compounds and to increase grain size through liquid phase assisted growth. The rapid thermal processing step mitigates undesirable solid phases and solid transformations predicted at low temperature.

(b) The I-V and DLTS measurements

Figure 2-3 shows the I-V curve for a UF CIS cell with 5% AM1.5G conversion efficiency, open-circuit voltage V_{oc} = 0.296 V, and fill factor $F.F.$ = 49.54%. The short-circuit current density, J_{sc}, for this cell is 34.65 mA/cm^2, which is an excellent value. The low fill factor is attributed to high sheet resistance in the CIS absorber. This can be improved by adjusting the Cu:In:Se composition ratio, especially the Cu to In ratio, and by creating a composition gradient to achieve band gap grading. The V_{oc} parameter is largely affected by the mid-gap defects in the space charge region.

DLTS and C-V measurements were performed on the UF CIS cells to characterize the deep-level defects in the cells. Figure 2-4 shows the C-V data obtained at different temperatures. The average hole density determined from the data was found to be approximately equal to 10^{15} cm^{-3}. From the C-T measurements values of the zero-biased capacitance C_0 at the DLTS peak temperatures of 150 K, 200 K, 290 K, and 300 K were found to be equal to 28.6 pF, 28.8 pF, 34.4 pF, and 37.7 pF, respectively.

Figure 2-5 (a) shows the DLTS spectra for this CIS cell using a reverse bias voltage, V_R = -0.5 V, a trap-filling pulse of 0.4 V, and a saturation pulse width of 10 ms. From the DLTS scans a deep-level majority carrier trap (hole trap) was observed at a temperature of around 290 K. Figure 2-5 (b) shows the corresponding Arrhenius plot, yielding an activation energy $E_a = E_v +$ 0.54 eV, which may be attributed to the Cu on In interstitial site assigned as E_{A6} in [1]. The average hole density at 290 K determined from the C-V measurements was found to be 2×10^{15} cm^{-3}. From the C-T and C-V data, the net trap density, N_T, was found to be equal to 4.6×10^{12} cm^{-3}.

To detect the possible minority carrier traps, a small forward bias was applied to the UF CIS cell to fill the minority carrier traps at room temperature, and the cell was then cooled down to 77 K to freeze out all the minority carrier traps. The cell was then heated up, and a pulse amplitude equal to 0.7 V, a reverse set-off voltage of -0.5 V and a saturation pulse width of 10ms were applied to the device to observe the capacitance change due to the minority carrier emission. The results are shown in Figure 2-6 (a), where a minority carrier (electron) trap peak was observed at a temperature of around 200 K in addition to the majority carrier trap reported in the previous paragraph. The companion Arrhenius plots for the minority-trap peak E_1 and for the majority-trap peak E_2 given in Figure 2-6(b) reveal that the activation energy for the minority (electron) trap is $E_1 = E_c$ - 0.97 eV, lying below the conduction band. A possible physical origin for this electron trap is attributed to the Cu vacancy (assigned as E_{A1} [1]). The trap density was estimated to be 1.3×10^{12} cm^{-3}.

In addition to the standard DLTS scans described above, we also performed optical DLTS scans on the UF CIS cell. A laser with wavelength of 532 nm was used to inject the minority carriers in the CIS cell with a reverse bias of - 0.5 V. Results of the optical DLTS scans are shown in Figure 2-7 (a),. It is noted that only the minority carrier traps with activation energies E_1 and E_2 were observed. As shown in the companion Arrhenius plot (Figure 2-7 (b)), the activation energy calculated for the E_1 electron trap is 0.16 eV below the conduction band. This electron trap is attributed to the In on Cu antisite defect In_{Cu}. The activation energy at 300 K for

a deeper electron trap could not be estimated since the peak shift does not follow the expected trend (*i.e.*, the shorter the rate window, the higher the temperature at which the peak appears). This may be attributed to the fact that the capture cross-section for this trap is a thermally activated process, and depends exponentially on the temperature by the expression,

$$\sigma = \sigma_0 \exp(-\Delta E / (kT))$$

where ΔE is the thermal activation energy of the capture cross section [7].

2.2.3.2 *Analysis of EPV CIGS cells*

Photovoltaic cells based on a thin-film CIGS absorber produced by Energy Photovoltaics Inc. (EPV) were also analyzed. The absorber films were grown by co-deposition in a proprietary physical vapor deposition system. Figure 2-8 (a) shows the DLTS spectra measured for a representative EPV CIGS cell, obtained using a reverse bias $V_R = $ -0.1V, a trap-filling pulse of 0.3 V, and a saturation pulse width of 10 ms. The EPV CIGS cell shows a deep majority-carrier (hole) trap at a peak temperature around 270 K. The DLTS peak shifts to higher temperatures with shorter rate windows. The activation energy calculated from the Arrhenius plot of Figure 2-8 (b) for this hole trap is $E_a = E_v + 0.94$ eV above the valence band edge, which may be attributed to the Se vacancy. The average hole density obtained from the C-V measurements at 270K is 3×10^{15} cm^{-3}. From the C-T data, value of C_0 was found equal to 301 Pf, and from Eq. (2) value of N_T was found equal to 6.5×10^{13} cm^{-3}.

2.2.3.3 *Analysis of NREL CIGS cells*

CIGS cells prepared at the National Renewable Energy Laboratory (NREL) using the three-stage process [8] in a physical vapor deposition system were also studied. In the first processing stage, a precursor $(In,Ga)_2Se_3$ layer is formed by the co-evaporation of In, Ga, and Se from elemental sources while holding the substrate at a temperature of approximately 260˚C. In the second stage, Cu and Se are co-evaporated to bring the overall composition to a near Cu-rich regime (corresponding to an elemental ratio Cu/(In+Ga) ranging from 0.97 - 1.08) at 560˚C. Before starting the third stage, the substrate is held under a Se flux while the temperature is ramped up to a new target. The third stage then commences, where In, Ga, and Se were added in an amount equal to one-ninth of the first stage to bring the overall composition back to a Cu-poor range at the substrate temperature used in the second stage. Finally, the substrate is cooled down to 350˚C and held under a Se flux for 20 minutes. The process requires very precise control of source flux.

The NREL CIGS cell used in the DLTS measurements has a total-area conversion efficiency of 19.2% (AM1.5G). Figure 2-9 (a) shows the result of DLTS scans carried out using a pulse amplitude equal to 0.4 V, and a reverse set-off voltage of -0.5 V. The figure reveals a minority carrier trap peak at near 100 K. From the companion Arrhenius plot of Figure 2-9 (b) it follows that the activation energy is $E_1 = E_c$ - 0.07 eV. A possible physical origin for this shallow electron trap is attributed to the Se vacancy (V_{Se}) [3]. The trap density was estimated to be 4.2×10^{13} cm^{-3}. The DLTS scans performed at higher temperatures show another positive peak;

however, the activation energy for this trap could not be resolved by heating the sample above 300 K due possibly to the large temperature dependence of the capture cross section for this trap.

From the result of the DLTS scans on the NREL CIGS cell, it is noted that the minority carrier traps are likely the dominant traps in this NREL cell. To detect other possible minority carrier traps, a small forward bias of 0.1 V was applied at room temperature, and the cell was then cooled down to 77 K to freeze the minority carriers. The cell was then heated with $V_R = -0.5$ V, a trap-filling pulse amplitude of 0.7 V, and a saturation pulse width of 10ms to observe the capacitance change due to the minority carrier emission. The DLTS results of Figure 2-10 (a) show three minority carrier traps, and features the emergence of a small peak around 250 K, which was not apparent in the previous DLTS spectra obtained under a 0.4 V pulse amplitude. The Arrhenius plot of Figure 2-10 (b) shows that the activation energy for the electron trap at 80 K is $E_1 = E_c - 0.14$ eV, lying below the conduction band edge. The trap density is estimated to be 2.54×10^{13} cm^{-3}. The electron trap observed at 80 K is possibly related to a vacancy on a Se site, which might be the same trap level as the one observed with the 0.4 V pulse amplitude scan shown in Figure 2-9 (a). The activation energy at 335 K could not be estimated since the peak shift does not follow the general trend, as discussed earlier. The minority carrier traps observed in the NREL CIGS cell are shallow traps, which are not effective recombination centers, as is evidenced by the high conversion efficiency obtained in this cell.

2.2.4   Conclusions

The DLTS and C-V measurements have been performed on three different CIS- and CIGS- thin-film solar cells fabricated by UF, EPV and NREL to identify the deep-level defects in these cells. The defect activation energies and trap densities were determined. Table 2-1 summarizes the DLTS data for the UF CIS cell prepared by using RTP on a bilayer precursor. A mid-gap hole trap and three electron traps were detected in this cell. The mid-gap hole trap was found to be the dominant deep-level defect in this cell. The observation of a low V_{oc} in this cell may be related to this deep-level defect, which serves as an effective recombination center in the absorber layer. Therefore, in order to improve the cell performance, it is necessary to improve the junction quality by eliminating this mid-gap defect in the CIS absorber. Adding Ga or S to create a band- gap gradient and to adjust the Cu:In:Se composition ratio could be a reasonable step for improving the cell performance.

The DLTS measurements on the EPV CIGS cell revealed a majority carrier (hole) trap with a quantified activation energy and trap density. The NREL CIGS cell showed three minority carrier traps, with one dominant shallow- trap. A summary of key results obtained for the EPV CIGS cell and the NREL CIGS cell are listed in Table 2-2. From a comparative analysis of Tables 2-1 and 2-2, we conclude that V_{Se} and In_{Cu} are the two main donor levels, that V_{Cu} is the shallowest acceptor level, and that Cu_{In} is the main mid- gap recombination center, which is consistent with the information from the literature [1-3]. The free energy associated with the formation of some defect structures is so small that little increase in thermodynamic potential results. Therefore, there is insufficient driving force to ensure their elimination under many synthesis conditions. The formation energies of these deep-level defects in the CIS and

CIGS cells, according to several researcher's calculations, are in the order of $V_{Cu} < In_{Cu} < Cu_{In} \approx In_{Cu} < V_{Se}$ [1,9]. However, the defect distribution largely depends on the composition. A more detailed investigation of the nature of deep-level defects and their role on the recombination process in CIGS materials could further elucidate the material behavior and contribute to improving the performance of CIGS cells.

2.3 Publications and presentations

1. Kerr, Lei L, X. Li, T. J. Anderson, R. Noufi, T. Coutts, O.D. Crisalle, and S. Li "Thermodynamic Modeling of F doping in SnO2", published in the 30th World Photovoltaic Specialist Conference Proceedings, Japan, (2003).

2. Kerr, Lei L, S.S. Li, S. W. Johnston, T. J. Anderson, O.D. Crisalle, J. Abushama and R. N. Noufi " Deep Level Transient Spectroscopy (DLTS) Characterization of Team CIGS Cells", published in the 20th NCPV Photovoltaics Program Review Proceedings, Golden, CO,(2003).

3. Kerr, Lei L, S.S. Li, S. W. Johnston, T. J. Anderson, O.D. Crisalle, J. Abushama and R. N. Noufi "Characterization of Deep-Level Defects in CIGS Cells by Deep Level Transient Spectroscopy (DLTS) Technique," submitted to Solid State Electronics, August, 2003.

2.4 References

[1]   S.B. Zhang, S-H Wei, and A. Zunger, *Phys. Rev. B*, Vol. 57, No. 16, pp 9642-9668 1998.

[2]   J.H. Schõn and E. Bucher, *Solar Energy Materials & Solar Cells*, Vol. 57, pp. 229-237, 1999.

[3]   H. Neumann and R.D. Tomlinson, *Solar Cells*, Vol. 28, pp.301-307, 1990.

[4]   T. Minemoto, *Solar Energy Materials & Solar Cells*, Vol. 67, pp. 83-88, 2001.

[5]   B.J. Stanbery, C.-H. Chang, S. Kim, S. Kincal, G. Lippold, S.P. Ahrenkiel, L. L. Kerr, T. J. Anderson, M.M. Al-Jassim, *Self Organized Processes in Semiconductor Alloys*, MRS Symposium Proceedings, Vol. 583, 195-200, 2000.

[6]   T. Gödecke, T. Haalboom, and F. Ernst, *Zeitschrift für Metallkunde*, Vol. **91**, No. 8 pp.622-662, 2000.

[7]   Sheng S. Li, *Semiconductor Physical Electronics*, Plenum Press, New York and London, 1993.

[8]   B. M. Keyes, P. Dippo, W. Metzger, J. AbuShama, and R. Noufi, *the 29th PVSC*, New Orleans, LA, 2002.

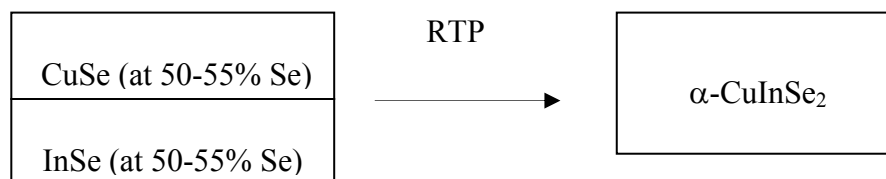[9]   H. Neumann, G. Kuhn, and W. *Moller, Physica Status Solidi (b)*, Vol. 144, pp. 565, 1987.

Figure 2-1.   Precursor structure consisting of stacked metal-Se layers subjects to rapid-thermal processing to produce a single-crystal α-CIS film.
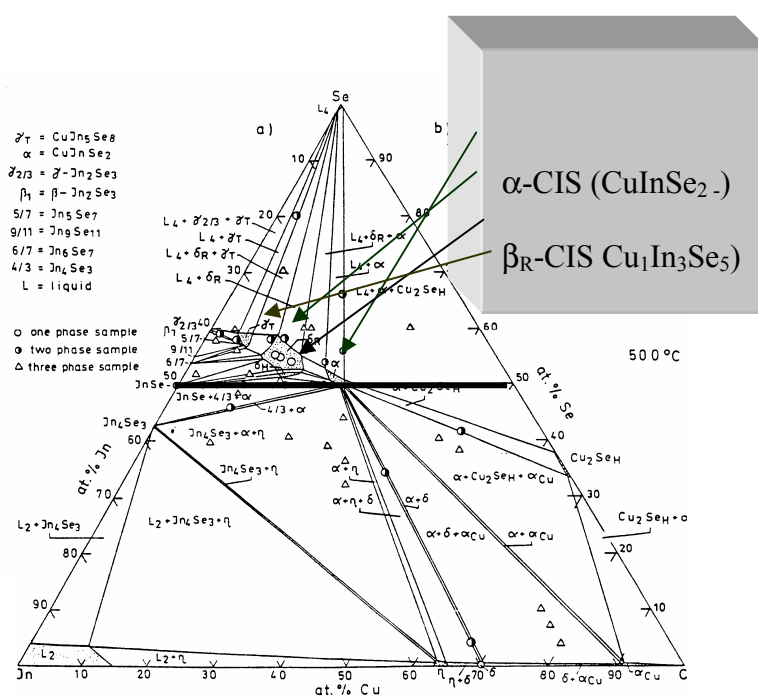

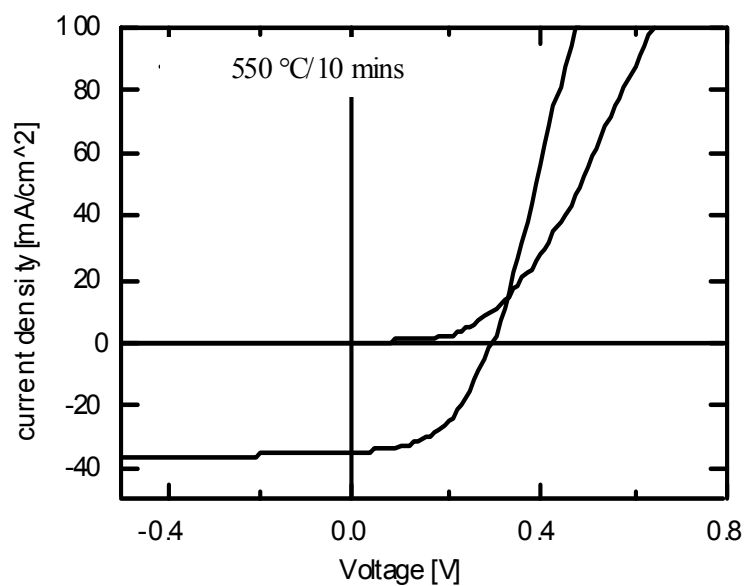Figure 2-2.   Isothermal composition phase diagram of Cu-In-Se system at 500˚C.

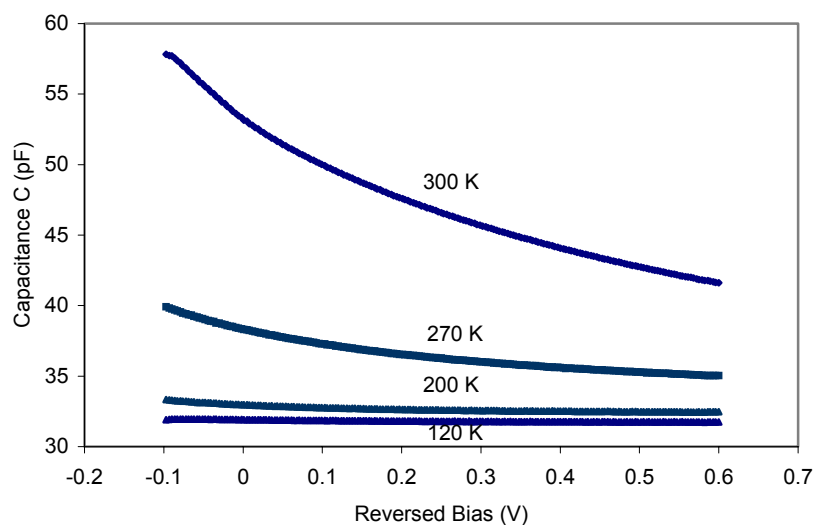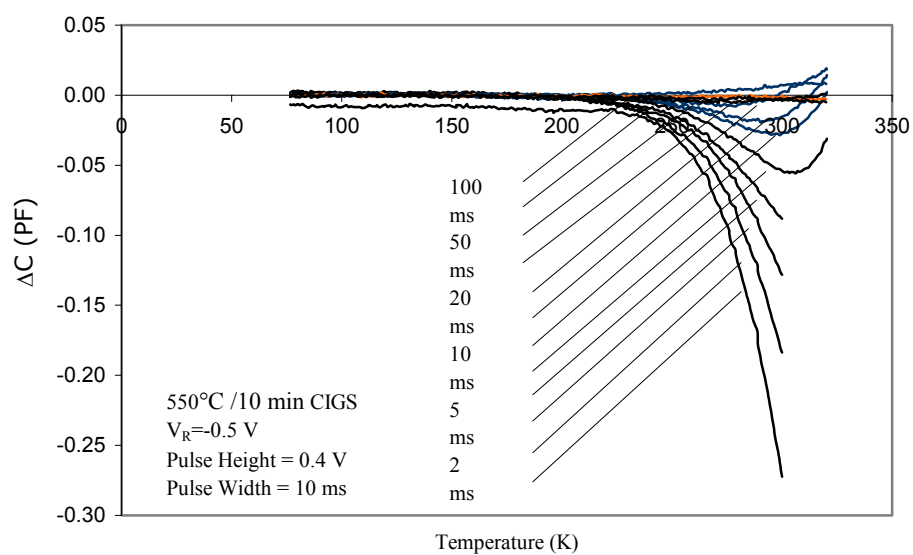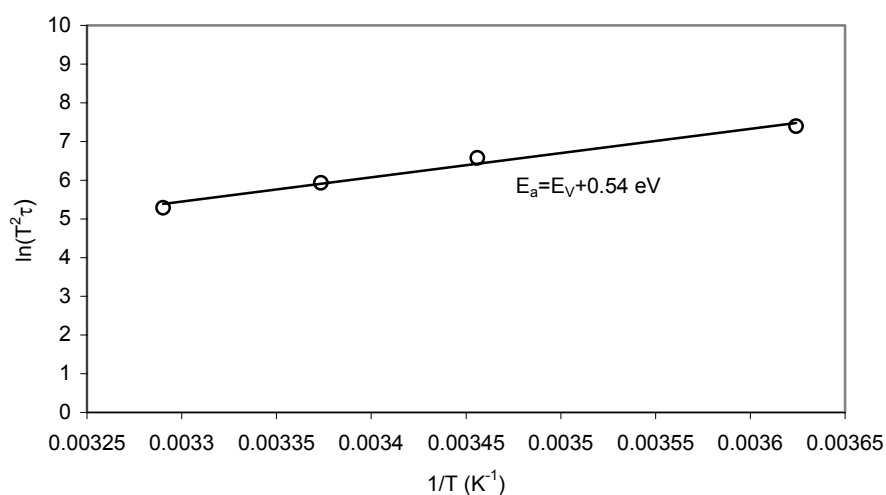Figure 2-3.   Dark- and photo- I-V curves for the UF CIS cell fabricated from the binary bilayer process.

Figure 2-4.   The capacitance-voltage curves for the UF CIS cell measured at different temperatures.

(a)

(b)

Figure 2-5. (a) DLTS scans for the UF CIS cell at different rate windows and at a reverse bias V_R = - 0.5 V, a pulse height of 0.4V, and a pulse width of 10 ms. (b) Arrhenius plot obtained from the DLTS data (a).
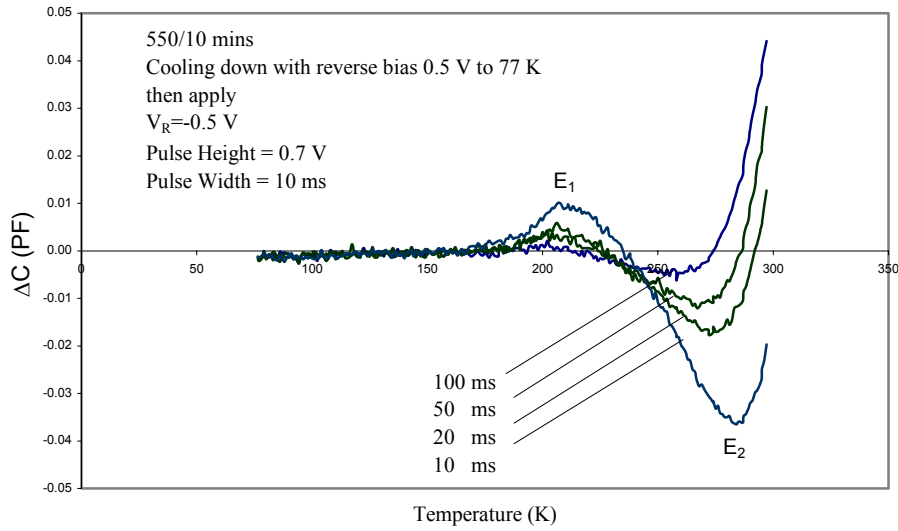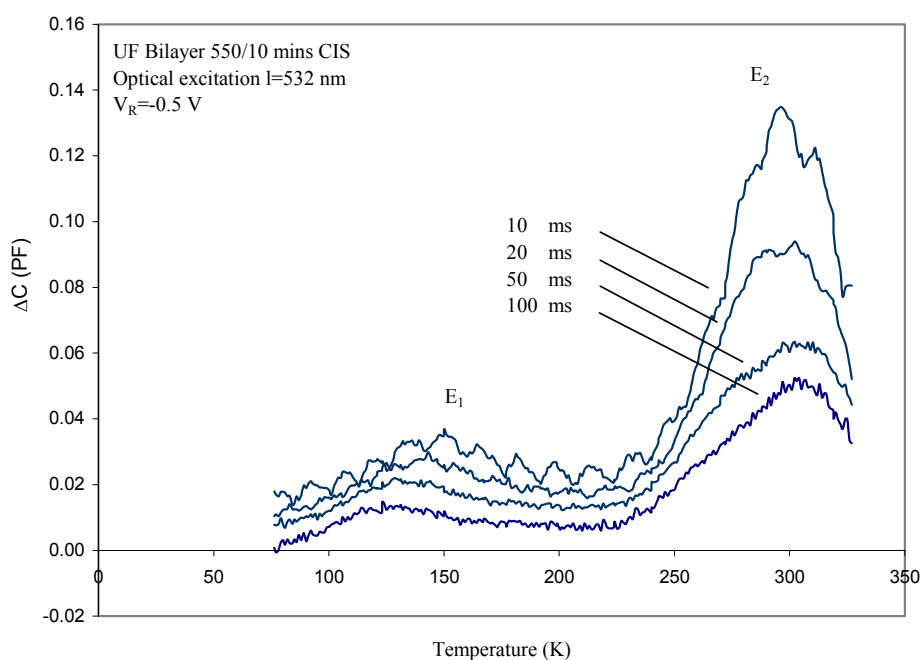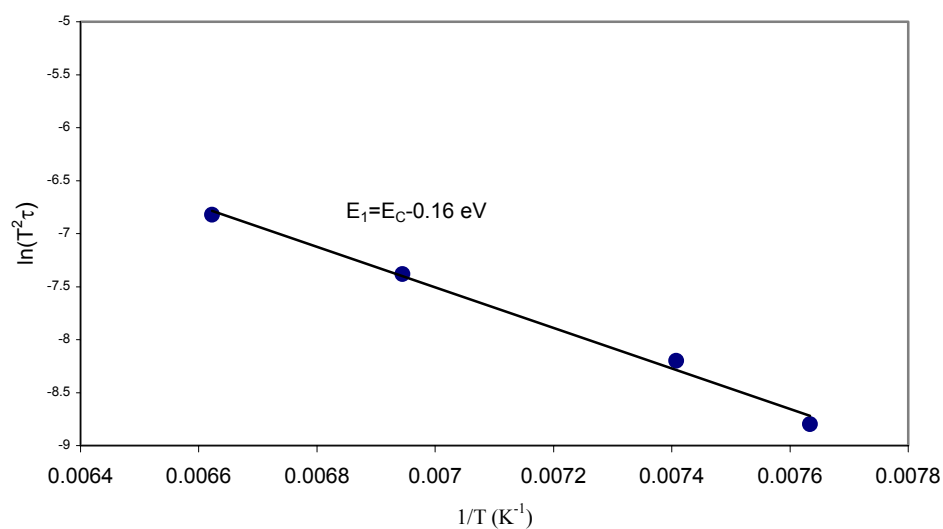
(a)
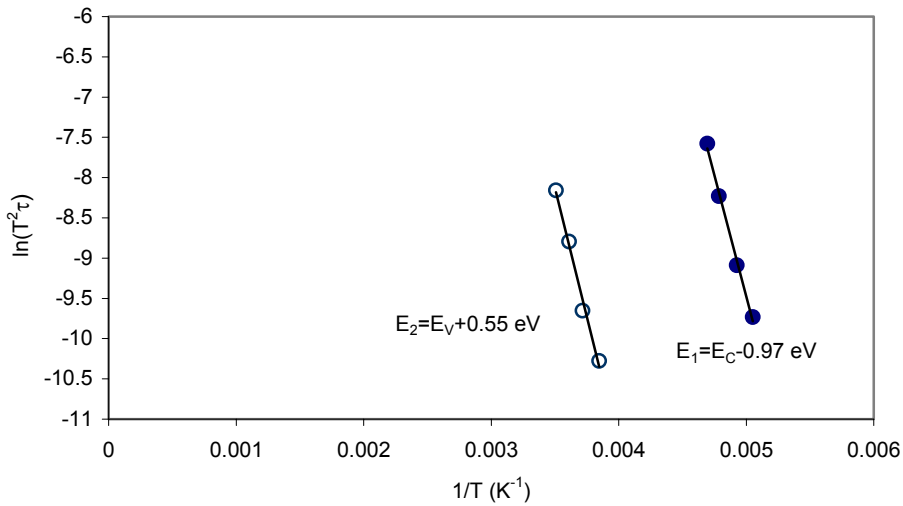
(b)

Figure 2-6. (a) DLTS scans for the UF CIS cell at a reverse bias $V_R = -0.5$ V, a pulse height of 0.7 V, and a pulse width of 10 ms. (b) Arrhenius plots obtained from the DLTS data (a).
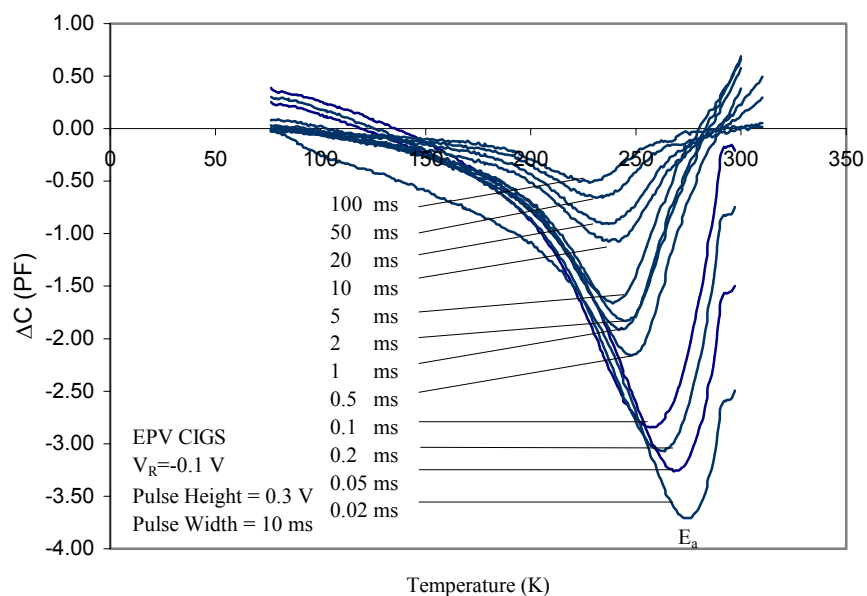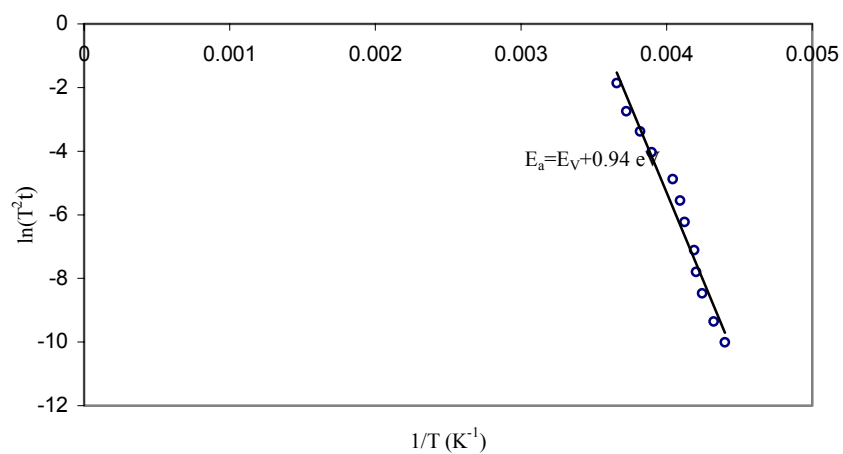
(a)

(b)

Figure 2-7. (a) Optical DLTS scans for the UF CIS cell measured at a reverse bias of $V_R = 0.5$ V, a wavelength $\lambda = 532$ nm, and a pulse width of 10 ms. (b) Arrhenius plot obtained from the DLTS data in (a).
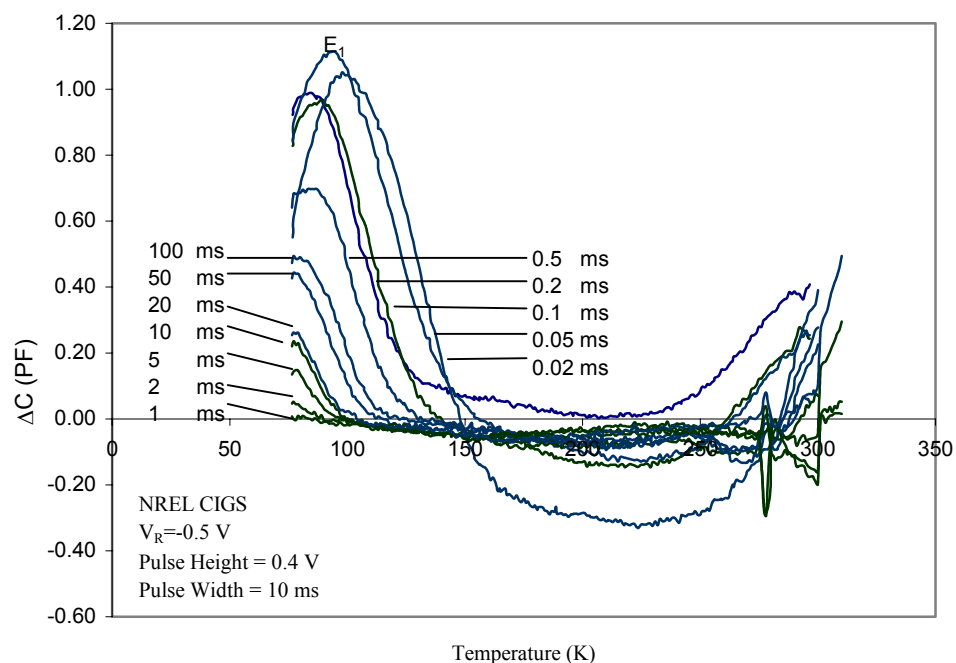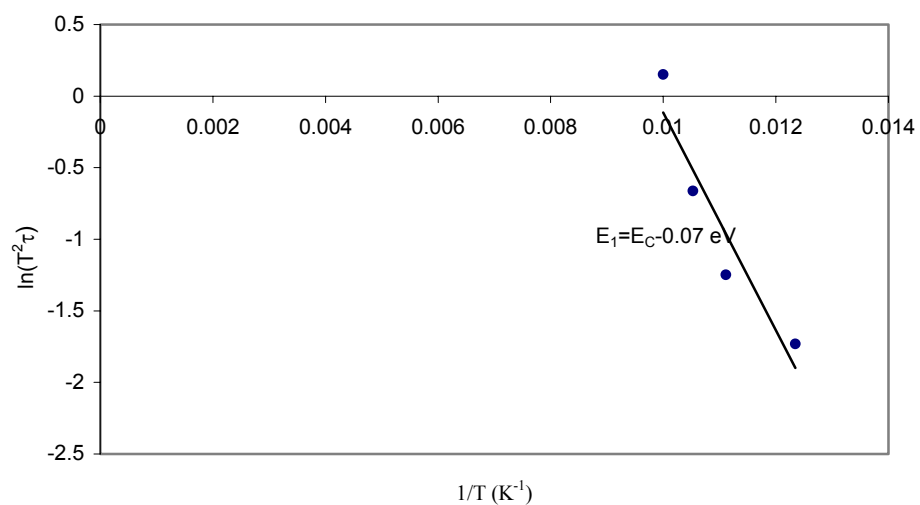
(a)

(b)

Figure 2-8. (a) DLTS scans for the EPV CIGS cell at a reverse bias of $V_R = -0.1V$, a pulse height of 0.3 V, and a pulse width of 10ms.) (b)Arrhenius plot obtained from the DLTS data in (a).
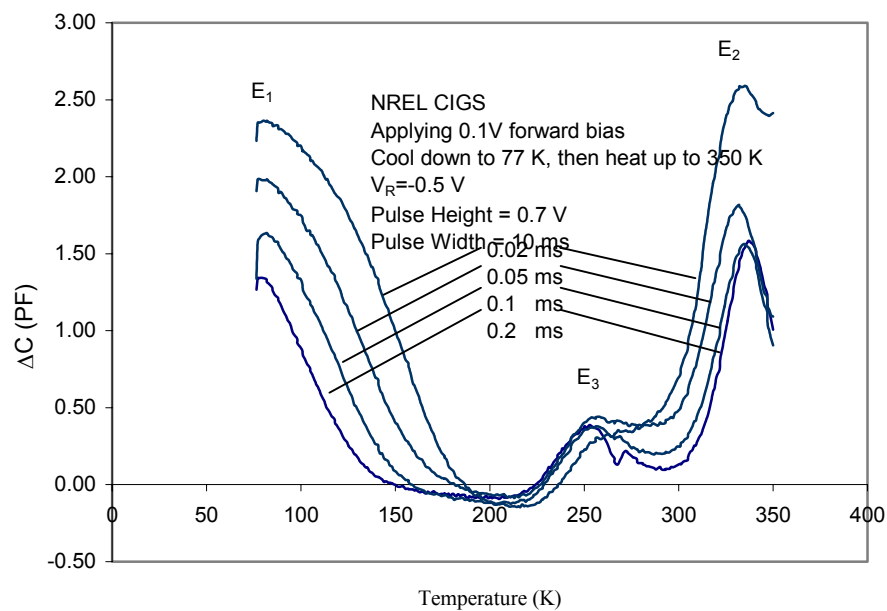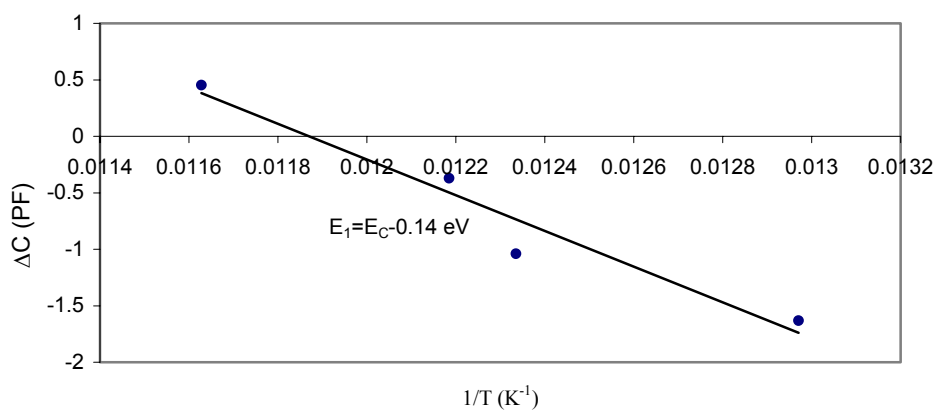
(a

(b)

Figure 2-9.   (a) DLTS scans for the NREL CIGS cell measured at a reverse bias V_R = -
0.5 V, a pulse height of 0.4 V, and a pulse width of 10 ms. (b) Arrhenius
plot obtained from the DLTS data in (a).

(a)

(b)

Figure 2-10. (a) DLTS scans for the NREL sample under forward bias injection (0.1V) and heat up, at a reverse bias V_R = -0.5V, a pulse height of 0.7V and a pulse width of 10 ms. (b) Arrhenius plot obtained from the DLTS data n in (a).

Table 2-1. Summary of the DLTS results for the UF CIS cell.

	$V_R = -0.5V$ $V_H = 0.4 V$ $W = 10 ms$	Cool to 77 K with reverse bias - 0.5 V, then apply $V_R = -0.5V,$ $V_H = 0.7 V$ $W = 10 ms$		Optical DLTS $V_R = -0.5V$ $\lambda = 532 nm$	
Approximate Peak Temperature (K)	290	290	200	150	300
DLTS Peak Sign	-	-	+	+	+
Trap Carrier Type	Majority	Majority	Minority	Minority	Minority
Trap Activation Energy E_a (eV)	$E_V +0.54$	$E_V +0.55$	$E_C -0.97$	$E_C - 0.16$	$E_C - 0.5$ *
Trap Density N_T (cm^{-3})	4.6×10^{12}	6.5×10^{12}	1.3×10^{12}	4.9×10^{12}	3.5×10^{13}
Possible Defect Origin	Cu_{In}	Cu_{In}	V_{Cu}	In_{Cu}	Cu_{In}
Capture Cross Section σ (cm^2)	1.39×10^{-14}	5.7×10^{-15}		1.2×10^{-18}	

* Estimated value based on a qualitative assessment of the position of the DLTS peak.

Table 2-2. Summary of the DLTS and C-V results for the EPV and NREL CIGS cells.

	EPV CIGS cell	**NREL CIGS cell**		
Approximate Peak Temperature (K)	270	100	250	335
Activation Energy (eV)	$E_v + 0.94$	$E_c - 0.067$		
DLTS Peak Sign	-	+	+	+
Trap Carrier Type	Majority	Minority	Minority	Minority
Net Hole Concentration N_a (cm^{-3})	3×10^{15}	2.25×10^{15}		
Trap Density N_T (cm^{-3})	6.5×10^{13}	4.2×10^{13}		
Possible Defect Origin	V_{Se}	V_{Se}		
Capture-Cross Section σ (cm^2)		6×10^{-18}		

3 Reaction kinetics of CuInSe₂ thin films grown from bilayer InSe/CuSe precursors

Participants: Timothy J. Anderson, Oscar D. Crisalle, and Sheng S. Li (Faculty Advisors), Suku Kim, Woo Kyoung Kim, Ryan M. Kaczynski, Ryan D. Acher, and S. Yoon (Graduate Research Assistants) and E. A. Payzant (Oak Ridge National Laboratory)**Objectives**

Study the reaction kinetics for the formation of $CuInSe_2$ thin films from a stacked bilayer precursor consisting of InSe and CuSe by means of in-situ high-temperature X-ray diffraction

3.2 Accomplishments

3.2.1 Introduction

Compound semiconductors based on $CuInSe_2$ are increasingly gaining acceptance as absorber-layer materials for thin film solar cells. The energy conversion efficiency of $CuInSe_2$–based solar cells has already reached that of the best solar cells made of crystalline silicon and of gallium arsenide. While there have been several studies on the mechanism for synthesizing $CuInSe_2$ absorber films, [1-4] the detailed reaction pathways are not fully understood, partly due to the complex phase evolution and defect chemistry present in the material system. Various binary and ternary phases can be simultaneously present in a Cu-In-Se ternary system, [3-5] and furthermore, phase transformations can occur during synthesis. Given that important transformations occur during the absorber formation process, *ex-situ* studies can fail to reveal key aspects of the reaction kinetics of $CuInSe_2$ formation. A more promising approach is to conduct an *in-situ* study of the phenomena using time-resolved, high-temperature X-ray diffraction analysis. This technique infers kinetic information from changes observed in the XRD data as a function of time as the film is heated. Careful analysis of *in-situ* XRD data with an advanced software JADE [6] permits quantitative investigation of the reaction kinetics.

The process followed to generate a $CuInSe_2$ film consists of first depositing a stack of two binary films that is a precursor of the absorber material $CuInSe_2$. Examples of stacked binary films are InSe/CuSe (*i.e.,* CuSe film grown over an InSe film that was grown on a substrate), InSe/Cu:Se (*i.e.,* an elemental mixture of copper and selenium deposited over an InSe film), and CuSe/In:Se. In all cases, the bottom binary films were grown over a thin (0.4 mm) sodium free glass substrate. The films were deposited in a modified molecular beam epitaxy reactor, and the total thickness of the stack was approximately 800 nm. The precursor stack is then heated to initiate a reaction leading to the formation of $CuInSe_2$ film, and the evolution of the reacting system is observed via *in-situ* high-temperature XRD.

The results of an *in-situ* isothermal time-resolved X-ray diffraction study of $CuInSe_2$ film growth from the binary precursor stack <u>InSe/CuSe</u> are reported in this article. Quantitative analyses were performed to estimate the reaction order and the apparent activation energy, as well as to elucidate mechanistic details of the film growth pattern.

3.2.2 Experiments

3.2.2.1 *Preparation of precursor films*

The deposition method used to grow the precursor films is called migration enhanced epitaxy (MEE), a variant of the classical molecular beam epitaxy (MBE) approach. As in MBE, an ultra high vacuum environment and effusion cells are employed to generate molecular beam fluxes of elemental sources. In MEE, however, the substrate is sequentially exposed to each source through revolution of a platen containing the substrate, rather than a simultaneous co-deposition from all the sources. Another important difference is that the rotating platen of the MEE system passes each substrate through a flux-free zone, namely a relaxation zone that enhances the potential for adsorbed atoms to migrate seeking the more energetically favored configurations. The direction of rotation can be either clockwise or counter-clockwise, so that the sequence of deposition may be reversed. It is also noted that the MEE reactor is capable of accommodating multiple substrates (up to nine) positioned on a large rotating platen. The base pressure of the system can be maintained as low as 8×10^{-9} Torr, and the pressure during deposition is in the range of 10^{-7} to 10^{-8} Torr depending on the operation conditions. Further details of the deposition technique and experimental apparatus are given elsewhere. [7]

For the InSe/CuSe bilayer structure, an indium selenide layer was first grown on to a thin (~0.4 mm) sodium-free glass substrate in the MEE system with a substrate temperature of approximately 250 °C. The films were made to have a slightly selenium-rich composition ([In]/[Se] ~ 0.95). Next, a copper selenide layer was deposited on the as-grown InSe layer at a lower temperature (~150 °C) to minimize potential reactions between the InSe and CuSe layers. The final stacked binary structure is depicted in Figure 3-1. Room temperature XRD data shows that the InSe phase is amorphous and that the CuSe phase is polycrystalline. The cross-sectional SEM image in Figure 3-1 (b) also shows that no grain structure is observed in the InSe layer, while the top CuSe layer has a large-grain structure (> 0.2 μm). The composition of the films was measured using inductively coupled plasma technique.

3.2.2.2 *Time-resolved high temperature X-ray diffraction*

Time-resolved, high-temperature X-ray diffraction data were collected while the precursor InSe/CuSe bilayers were isothermally reacted in stagnant air. The experimental set point temperature was in the range 220 to 270 °C. Initially, the samples were mounted on a platinum strip heater, and XRD data were collected at room temperature. Then the samples were heated at rate of 120 °C /min until the temperature reached a value 20 or 30 °C below the desired target temperature. The temperature was allowed to stabilize, and then the system was again heated at 120 °C /min until the target temperature was reached. XRD data was collected for a period of time, typically an hour, at the target temperature. All substrates were then subjected to a final isothermal temperature treatment at 340 °C for 30 minutes to ensure the completion of all reactions (*i.e.,* accomplish a total conversion of the reactants into the final product phase). XRD data were also collected during this last isothermal treatment.

The high-temperature X-ray diffractometer used in this study consisted of a Scintag PAD X

vertical θ/θ goniometer, a Buehler HDK 2.3 furnace, and an mBraun linear position sensitive detector (LPSD). The LPSD was centered at 28° 2θ and covered a 10° range (*i.e.,* from 23 to 33°). In contrast to conventional X-ray point scanning detectors that perform the scanning step-by-step from lower to higher angles, the LPSD collects the XRD data simultaneously over the 10° window, dramatically shortening the data collection time. This permits *in-situ* time-resolved studies of phase transformations, crystallization, and grain growth. The collection time for the 10° 2θ window was set to be either 19.5 or 34.5 seconds, depending on the temperature range. Figure 2 displays the time-resolved XRD data collected for a sample reacted isothermally at 218 °C. To obtain the fractional reaction (α), the areas for the CuSe (006) peak and the CuInSe$_2$ (112) peak were estimated from the diffraction data using the JADE software. [6] The values were normalized assuming that the reactants are completely transformed to crystalline CuInSe$_2$ after each run, and that the texture of the CuInSe$_2$ does not appreciably change through the entire heating process. Figure 3 displays the fractional reaction of CuInSe$_2$ formation as a function of time for all the temperatures considered, while Figure 4 shows the consumption of CuSe.

Non-isothermal heating was used to investigate the phase evolution of the samples, as follows. The InSe/CuSe samples were heated to several target temperatures. The samples were held at isothermal conditions for 15 minutes, and sequential longer-range (20-55° 2θ) high-temperature X-ray diffraction scans were collected every 85 seconds. After 15 minutes, the temperature was raised to the next target value, and the process was repeated. The longer-range high-temperature X-ray diffraction scans were used to trace all the intermediate phases and their transformations, and they were realized by combining high-temperature X-ray diffraction data from four discrete LPSD positions.

3.2.2.3   C. Temperature calibration

Since the thermocouple used to measure the temperature was welded to the bottom of the strip heater, a temperature calibration procedure was required to estimate the actual film temperature. Accurate measurement of the thin film temperature was achieved by calibrating to the known thermal expansion of silver, chosen for its high coefficient of thermal expansion (19.5×10^{-6} /K). [8] A fine silver powder was carefully dispersed on the surface of a 0.4 mm glass substrate, and was then annealed at a temperature well above the range of the experimental conditions to produce a solid thermal contact and minimize undesired thermal effects during the calibration run. For each run, a control program was set to heat the samples at 60 °C/min to the target temperatures, and followed by a hold period until the thermocouple reading became constant. The position of the silver (331) peak was measured from room temperature to 440 °C (thermocouple reading) and used to calculate the lattice parameter *L(T)* from the expression

$$L(T)=d_{hkl}\sqrt{h^2+l^2+k^2} \tag{3-1}$$

where *h*=3, *k*=3, and *l*=1, and d_{hkl} is the spacing between atomic planes inferred from the peak position.

The thermal expansion ratio was taken from the correlation reported by Touloukian *et al.* [9]

$$\frac{L(T)-L_0}{L_0} = -0.515+1.647\times10^{-3}T+3.739\times10^{-7}T^2+6.283\times10^{-11}T^3 \tag{3-2}$$

where L_0 is the lattice parameter of silver at $T_0 = 293$ K, and T is measured in degrees Kelvin. The correlation is valid in the temperature range 200 to 1200 K. Substituting (3-1) into (3-2) yields

$$\frac{d_{hkl}\sqrt{h^2+l^2+k^2}-L_0}{L_0} = -0.515+1.647\times10^{-3}T+3.739\times10^{-7}T^2+6.283\times10^{-11}T^3 \quad (3\text{-}3)$$

Since the left-hand side of (3-3) contains known quantities, the surface temperature of the film can be calculated. Table I displays the deviation between the thermocouple reading and the temperature of the specimen estimated by the thermal expansion method. The difference between the thermocouple reading and corrected temperature reported in Table I is in the range 52 to 59 °C, and this difference is largely attributed to the low thermal conductivity of the glass substrate. The calibration experiments were replicated, and the results were reproducible within ±2 °C.

3.2.3 Results and Discussion

According to the room temperature XRD analysis, the top CuSe layer is a homogeneous crystalline phase with an atomic ratio 1:1, and the bottom InSe layer is either an amorphous or a nanocrystalline phase with an atomic ratio 1:1.05. The expected interfacial reaction is

$$CuSe + InSe \rightarrow CuInSe_2 \qquad (3\text{-}4)$$

Time-resolved high-temperature X-ray diffraction scans showed that the transformations produce a crystalline $CuInSe_2$ phase product, as expected from reaction (3-4), and that there is no evidence of other intermediate phases.

It is well known that in multilayer thin film systems, the product layer grown at the initial interface of the reactants acts as a nucleation barrier as well as a diffusion barrier. The nucleation barrier often forces a meta-stable amorphous phase to form prior to any crystalline phase. [10,11] Amorphous and crystalline phases may grow simultaneously during subsequent reaction. [12] Additional heating may cause a further transformation of the amorphous phase to a crystalline one and may also induce additional nucleation reactions.

Analysis on the time dependent XRD peaks shows that both the product phase ($CuInSe_2$) formation and crystalline reactant-phase (CuSe) consumption follow the same deceleratory reaction trend (Figures 3-3 and 3-4), which can be attributed to diffusion-controlled reaction kinetics. Figure 3-5 demonstrates that the sum of the mole fractions of the CuSe reactant and of the product quickly falls below unity during the early stage of the isothermal reacting process, because the rate of the CuSe consumption is faster than that of the $CuInSe_2$ formation. This implies that there is an intermediate phase present before the final product is fully formed. As the long-range, high-temperature X-ray diffraction scans showed no evidence of intermediate crystalline phases, the hidden intermediate phase is most likely amorphous $CuInSe_2$. Under this perspective, during the initial stage of the heating process the sum of the mole fractions falls significantly below unity, an effect that can be explained by the formation of an amorphous $CuInSe_2$ phase, which is initially prevented from evolving into a crystalline phase due to the nucleation-barrier effect. As the heating energy progressively overcomes the nucleation barrier, the $CuInSe_2$ material also progressively crystallizes, and the sum of mole fractions rises towards unity. The combined amorphous and crystalline $CuInSe_2$ interfacial layer also acts as a diffusion

barrier, opposing the one-dimensional diffusion of the reactants shown on the left-hand side of reaction (3-4). In summary, the InSe|CuInSe$_2$|CuSe structure introduces both a nucleation and a diffusion barrier. As the isothermal reaction continues, the sum of the mole fractions rapidly increases towards unity (Figure 3-5). This indicates that the amorphous phase fully transforms into a crystalline phase. The XRD data of Figure 3-5 show that for all cases the amorphous phase is completely consumed during the final heating step at 340 °C. Further study, perhaps including detailed microscopic analysis, will be needed to better understand the initial stage of the growth mechanism.

The analysis proposed above is consistent with the prevailing suggestions on the growth mechanism documented in the literature. It has been claimed that during the initial steps of solid-solid reaction, the formation of product is rapidly accomplished on the attainment of reaction temperature. [13] The initial nucleation reactions at the original interface of the bilayer structure may occur even before the temperature reaches the target values likely via a fast two-dimensional growth mode, rapidly evolving to impingement. This gives rise to a nucleation barrier that would dramatically reduce the nucleation rate, so that the nucleation reaction is expected to be rapidly deceleratory.

The growth of the CuInSe$_2$ phase is governed by the planar nature of the precursor film structure. During the early stage of the reaction, heterogeneous nucleation and fast saturation is expected to occur at the original interface. The in-plane material transport is likely to be sustained by rapid interface diffusion, so that at the initial instants the growth at the original interface plane may not be limited by diffusion. The nucleated CuInSe$_2$ phase grows and coalesces into a continuous layer. After this initial transient stage, the product layer thickens by a diffusion-limited process that is likely one-dimensional and perpendicular to the original interface. [10,12] The subsequent growth of the product phase, the main reaction stage, is now controlled by the diffusion of one or more species through the product layer.

The kinetics of the growth reactions in terms of activation energy and reaction order have been investigated using two solid-state reaction models, namely, the Avrami and parabolic rate models. Avrami analysis is a widely used method for the preliminary identification of the growth rate law. It has been shown that the method yields satisfactory fits to relevant experimental data. [13] The transformation kinetics under isothermal reaction is described by

$$\alpha = 1 - \exp\left(-(kT)^n\right) \tag{3-5}$$

or equivalently, by

$$\ln\left(-\ln(1-\alpha)\right) = n\ln T + n\ln k \tag{3-6}$$

where the fractional reaction α represents the volume fraction transformed, k is the kinetic rate constant, and n is the Avrami exponent. This analysis has been advocated by Hulbert, [14] who showed that the Avrami exponent can vary between 0.5 and 1.5 in the case of one-dimensional diffusion-controlled reactions. The value of n is close to 0.5 if the nucleation is instantaneous, and close to 1.5 if the nucleation rate is constant throughout the reaction. It is well known that thickening of thin planar structures after complete edge impingement is realized through one-dimensional growth mode. [15]

Figure 3-6 displays the Avrami plots for the isothermal reaction of the precursor films at different temperatures. Data were taken only for $0.1 < \alpha < 0.95$ to minimize experimental errors.

Clearly, the data are well fit by the Avrami model (3-6). Table II shows the kinetic rate constant and Avrami exponent estimated from the plot. The value of the Avrami exponent is between 0.5 and 0.8, and consistently increases with temperature. This indicates that the growth mechanism is through one-dimensional thickening of the product layer, and that it is also diffusion-controlled. The increase of the *n* value with temperature is believed to be caused by the enhancement of the nucleation processes with temperature. Higher temperature conditions can overcome the nucleation barrier, so that the nucleation rate during the subsequent growth of the product phase increases with temperature. The temperature effect on the Avrami exponent has been previously reported via simulation studies. [16]

The Avrami parameters and the Arrhenius equation

$$k = A\exp\left(-E_a/RT\right) \tag{3-7}$$

were used to estimate the apparent activation energy E_a for the CuInSe$_2$ formation reaction from the bilayer precursor films. The Arrhenius plot shown in Figure 3-7 yields an estimated value of $E_a = 66.0$ kJ/mol.

A second study was performed based on a diffusion-controlled rate law. The simple parabolic kinetic model

$$\alpha = (kt)^{1/2} \tag{3-8}$$

describes well a process where the interface area is constant and the diminution of reaction rate is a consequence of increasing thickness of the diffusion barrier.

This rate expression has been shown to be obeyed by a one-dimensional diffusion process, such as oxidation of metals, where the reactant is in the form of a thin sheet. Figure 8 shows the plot of $\ln \alpha$ vs. $\ln t$ for the same XRD data used in the Avrami analysis. Table III gives the slope of each curve and the resulting kinetic rate constants extracted from the slopes of the plot. The slope is approximately equal to 0.5 for all the runs throughout most of the reaction period, which strongly indicates that the reaction is one-dimensional diffusion controlled. This result is consistent with the conclusions reached from the Avrami analysis. The Arrhenius equation and the parabolic law parameters were used to produce another estimate of the apparent activation energy using (7). The result yielded the apparent activation energy $E_a = 65.2$ kJ/mol, which is consistent with the value $E_a = 66.0$ kJ/mol obtained from the Avrami analysis. Hence, the results from two different analyses are consistent and lead to an identical conclusion, namely that the reaction is one-dimensional diffusion controlled.

3.2.4 Conclusions

Time-resolved, high-temperature X-ray diffraction analysis has been successfully employed to conduct quantitative analyses of the reaction kinetics of the CuInSe$_2$ phase formation from bilayer InSe/CuSe precursor films. Transformation from the precursor films into the final phase was clearly observed by *in-situ* X-ray diffraction scanning during isothermal heating. The data analysis based on the Avrami and the parabolic rate law models support the conclusion that the reaction mode is one-dimensional diffusion controlled. The estimated apparent activation energies from these analyses are 66.0 kJ/mol, and 65.2 kJ/mol, respectively.

Careful analysis of XRD data showed that there was a non-crystalline intermediate phase, most likely amorphous $CuInSe_2$, during the initial stage of the isothermal heating process. The combined amorphous and crystalline $CuInSe_2$ interfacial layer functions as a diffusion barrier as well as a nucleation barrier.

3.3 References cited

[1]   J.R. Tuttle, M. Contreras, M.H. Bode, D. Niles, D.S. Albin, R. Matson, A.M. Gabor, A. Tennant, A. Duda, and R. Noufi, J. Appl. Phys. **77**, 153 (1995).

[2]   A. Rockett, F. Abou-Elfotouh, D. Albin, M. Bode, J. Ermer, R. Klenk, T. Lommasson, T.W.F. Russell, R.D. Tomlinson, J. Tuttle, L. Stolt, T. Walter, and T.M. Peterson, Thin Solid Films **237**, 1 (1994).

[3]   R. Klenk, T. Walter, H.W. Schock, and David Cahen, Adv. Mater. **5**, 114 (1993).

[4]   V. Nadenau, D. Braunger, D. Hariskos, M. Kaiser, Ch. Köble, A. Oberacker, M. Ruckh, U. Ruhle, D. Schmid, T. Walter, S. Zweigart, and H.W. Schock, Prog. Photovoltaics: Research and Applications **3**, 363 (1995).

[5]   C.-H. Change, Ph.D. Thesis, University of Florida (1999).

[6]   JADE, a program for powder diffraction data analysis, Materials Design Inc., Livermore, CA, USA.

[7]   B.J. Stanbery, S. Kincal, S. Kim, C.H. Chang, S.P. Ahrenkiel, G. Lippold, H. Nuemann, T.J. Anderson, and O.D. Crisalle, J. Appl. Phys. **91**, 3598 (2002).

[8]   J.A. Brand, and H.J. Goldschmidt, B.S.A. Group Research Center Sheffield, GRC/G 1109, (1955).

[9]   Y.S. Touloukian, R.K. Kriby, R.E. Taylor, and P.D. Desai, Thermophysical Properties of Matter **12**, 298 (1977).

[10]   E. Ma, C.V. Thompson, and L.A. Clevenger, J. Appl. Phys. **69**, 2211 (1991).

[11]   W.L. Johnson, Prog. Mater. Sci. **30**, 81 (1986).

[12]   L.A. Clevenger, and C.V. Thompson, J. Appl. Phys. **63**, 1325 (1990).

[13]   C.H. Bamford, and C.F.H. Tipper, Reactions in the solid state, Elsevier Scientific Publishing Company, Amsterdam, New York, (1980).

[14]   F. Hulbert, J. Br. Ceram. Soc., **6**, 11 (1969).

[15]   J.W. Christian, *The theory of transformations in metals and alloys, part* I, Pergamon press, New York, (1975), p. 542.

[16]   R. Pascual, M. Sayer, A.Lo, S. Herbert, L.C. Rolim, and N. Townley, J. Appl. Phys. **79**, 493 (1996).

Table 3-1. Thermocouple reading and corrected temperature of the specimen measured by the thermal expansion method.

Thermocouple reading [°C]	Specimen temperature [°C]
270	218
290	236
310	253
330	271

Table 3-2. Estimated rate constants and Avrami exponents for the $CuInSe_2$ formation from bilayer precursor films.

Temperature [°C]	k [s^{-1}]	Avrami exponent n
218	0.000298	0.573
236	0.000562	0.649
253	0.000945	0.722
271	0.00148	0.760

Table 3-3. Estimated rate constants and the exponents based on the parabolic rate law for the $CuInSe_2$ formation from bilayer precursor films.

Temperature [°C]	k [s^{-1}]	Avrami exponent n
218	0.000116	0.446
236	0.000190	0.450
253	0.000347	0.502
271	0.00539	0.514
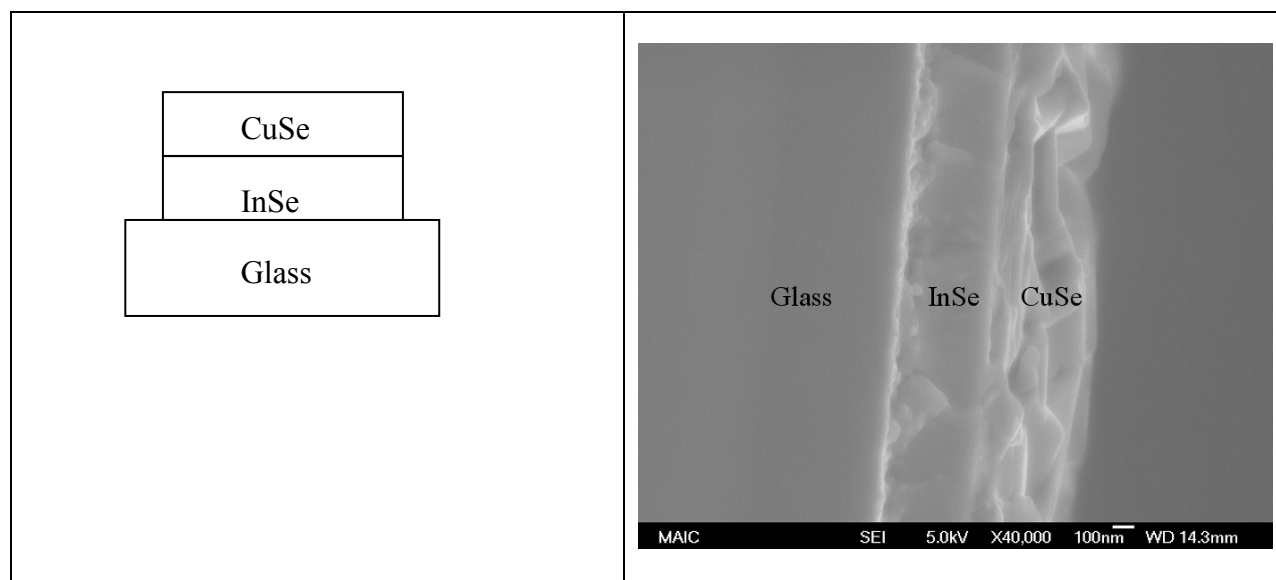
Figure 3-1. Bilayer InSe/CuSe precursor used in the study: (a) schematic diagram, (b) cross-sectional SEM image (×40,000).
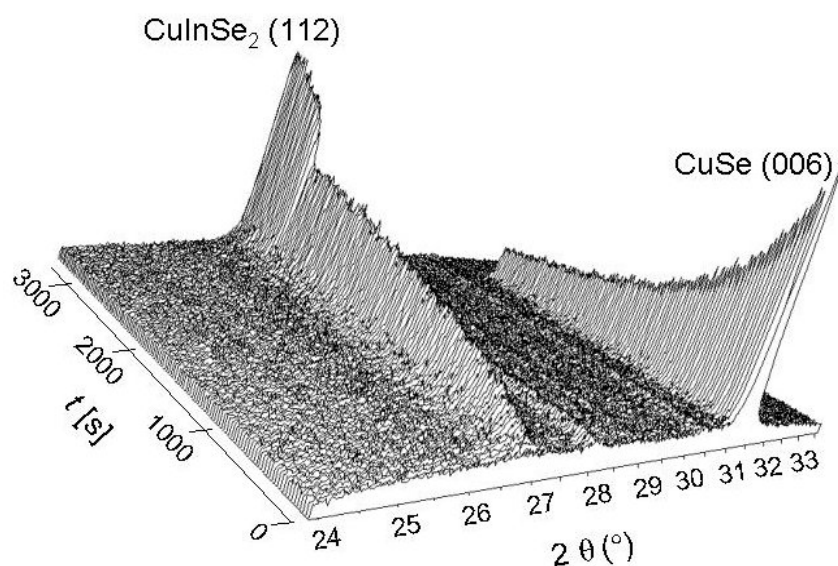
Figure 3-2. Time-resolved *in-situ* X-ray Diffraction data for isothermal reaction at 218 °C. The last 20 data points were collected while reacting at 340 °C for 30 minutes.
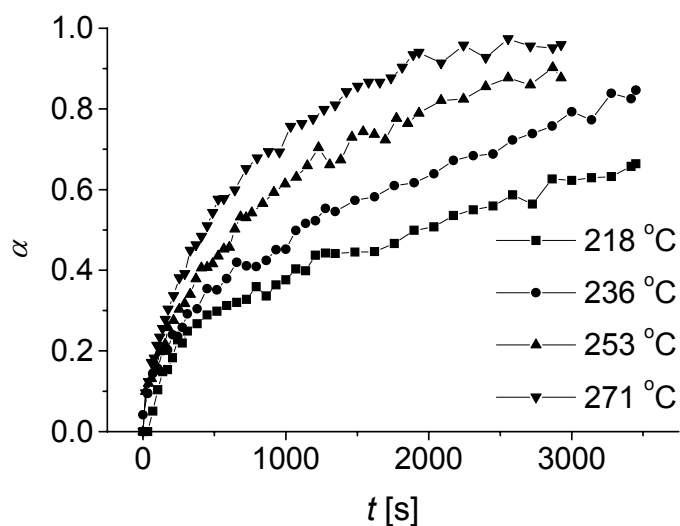
Figure 3-3. Fractional reaction α of CuInSe$_2$ formation during isothermal processing as a function of time and temperature.
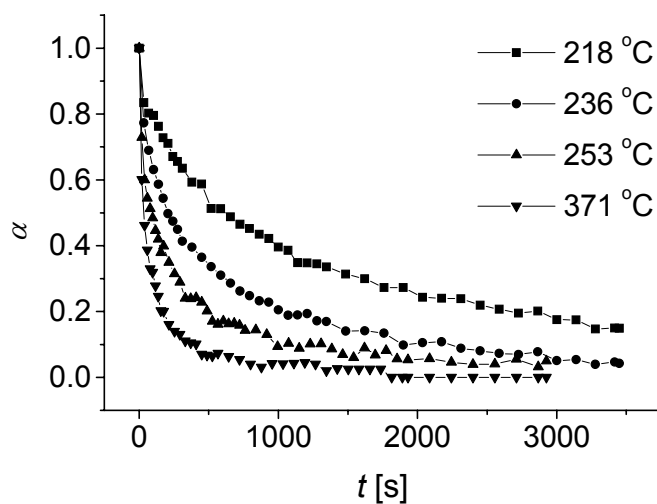

Figure 3-4. Fractional reaction α of CuSe transformation during isothermal runs as a function of time and temperature.
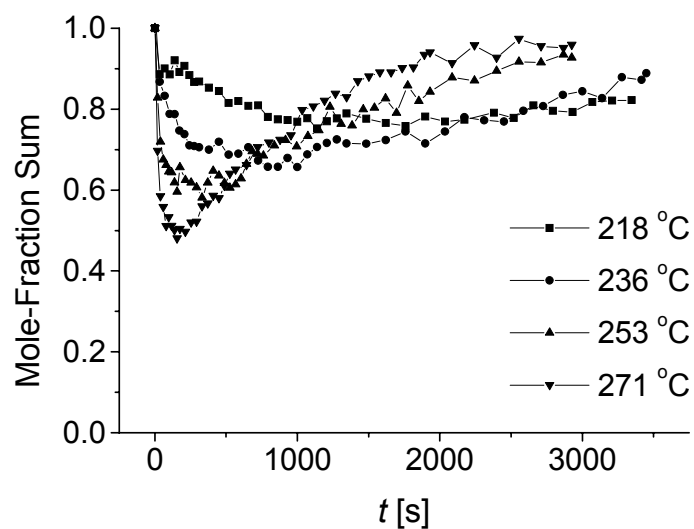
Figure 3-5. Sum of the mole fractions of the crystalline reactant (CuSe) and product (CuInSe$_2$) during isothermal reaction.
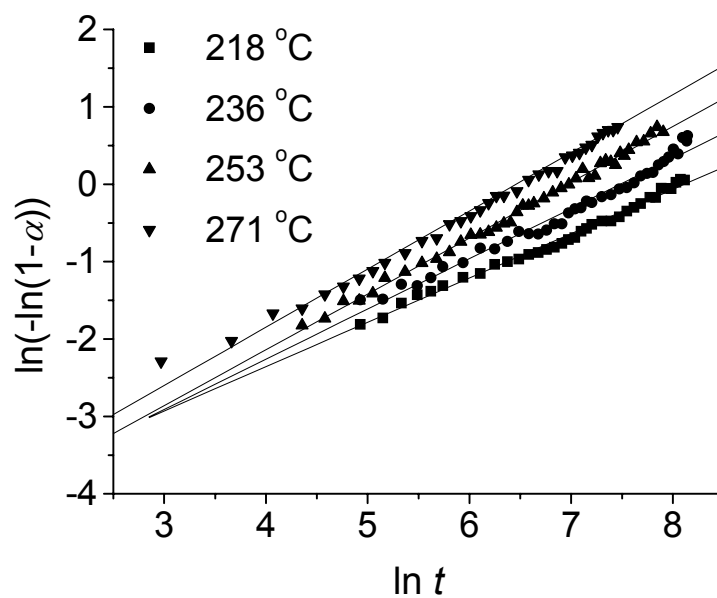
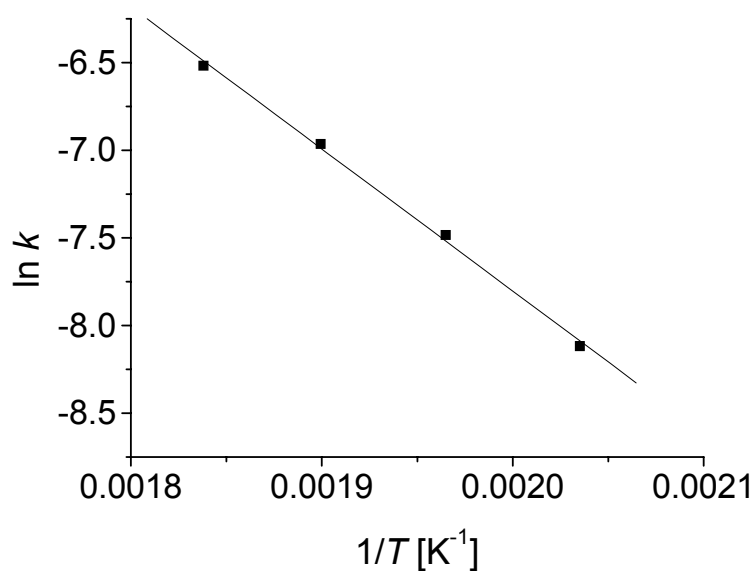Figure 3-6. Avrami plots for the isothermal reactions at different temperatures.

Figure 3-7. Arrhenius plot for the isothermal reactions based on Avrami analysis. The apparent activation energy for the CuInSe$_2$ growth reaction is $E_a = 66.0$ kJ/mol.

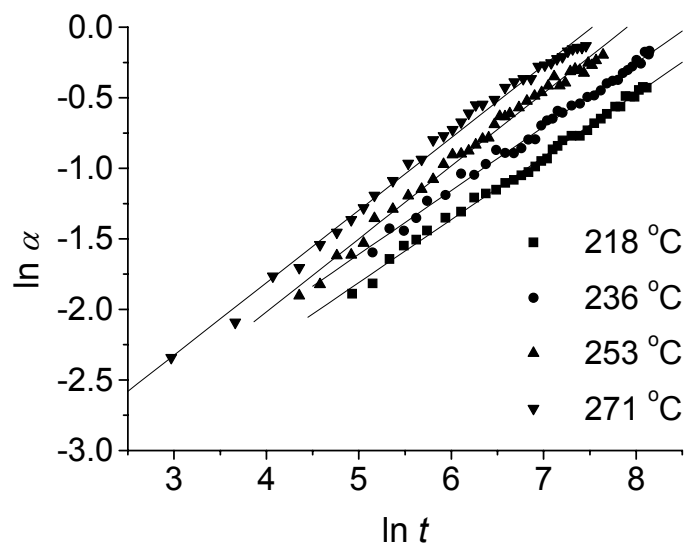Figure 3-8. Fractional reaction plots based on the parabolic rate law for isothermal reactions at different temperatures.
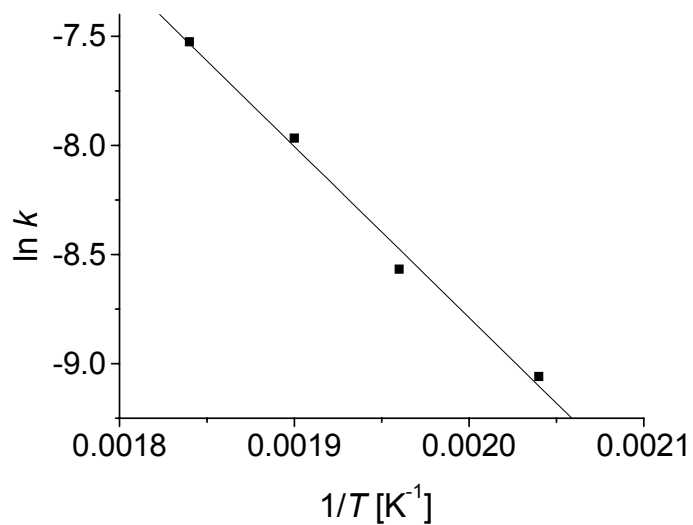
Figure 3-9. Arrhenius plot for the isothermal reactions based on parabolic rate law analysis. The apparent activation energy for the CuInSe$_2$ growth reaction E_a = 65.2 kJ/mol.

4 Thermodynamic Modeling of Fluorine Doping in SnO₂

Participants: Timothy J. Anderson, Oscar D. Crisalle, Sheng S. Li (Faculty Advisor), and Lei L. Kerr (Research Assistant), Xiaonan Li, T. Coutts, R. Noufi.

4.1 Objectives

A model is developed to estimate the equilibrium fluorine solubility in fluorine-doped tin oxide (FTO) as a function of temperature and of the partial pressure of dopant precursor.

4.2 Accomplishments

4.2.1 Introduction

Fluorine-doped tin oxide (FTO) films are widely used as a transparent conductor in solar cell applications. This transparent conductive oxide (TCO) material can be prepared by several manufacturing techniques, including sputter deposition, chemical vapor deposition (CVD), and spray pyrolysis deposition. For solar cell applications it is desirable for the TCO to exhibit both high electrical conductivity and high transparency. It is well known that high fluorine concentrations in the film increase the electrical conductivity, but unfortunately at the same time the film transparency decreases. A method for estimating the solubility of F in SnO_2 would therefore be most useful for establishing optimal processing conditions. In this study the Delta Lattice Parameter (DLP) modeling approach [3] was used to estimate the interaction energy of the pseudobinary SnF_2-SnO_2 solid solution. The resulting model then allows a reasonable estimation of the extent of F incorporation in a SnO_2 film during CVD, assuming that the film growth is mass transfer limited and that the growth interface is at equilibrium. Experimental observation available in the literature [9][10] are used to determine the components present in the gas phase, yielding a key piece of information needed to populate the database that serves as the basis for a thermodynamic analysis using Thermo-Calc software package [1]. Thermo-Calc was developed in 1981, and is a powerful and flexible tool for performing various kinds of thermodynamic and phase diagram calculations, including analysis of CVD-grown thin films.

This paper is organized as follows. Section 4.4.2 describes the experimental and calculation procedure followed, including a discussion of the relevant thermodynamic models involved, the evaluation of the interaction parameters needed for the models, the calculation of fluorine solubility, and an analysis of the effect of various CVD parameters in solubility. Section 4.2.3 summarizes the results along with a comprehensive discussion. Finally, section 4.2.4 offers concluding remarks.

4.2.2 Experimental and Calculation Procedure

FTO films were deposited on a glass substrate using a gas mixture containing a F precursor, tetramethyltin (TMT), and oxygen, in a low-pressure chemical-vapor deposition

(LPCVD) reactor. The three precursors considered were $CBrF_3$, CIF_3, and CF_4. The reactor uses more than twenty infrared lamps for heating of the substrate. The gases were introduced into the reaction chamber via two injectors located on the top and bottom of an end-cap flange. Films were grown under various temperatures, and various partial pressures of precursor gases. The resulting films were characterized via Hall effect measurements using a Bio-Rad HL5500 Hall system to determine the carrier concentration. In addition, SIMS profiles using a CAMECA IMS 5f system were taken to estimate the F content of the deposited films.

4.2.2.1 Thermodynamic Models

The two phases, namely, gas and FTO solid solution are in equilibrium at growth interface assuming the film growth is a mass transfer limited process. Thermodynamic model for both phases are needed to construct a Gibbs energy database in order to perform equilibrium calculation. The development of a thermodynamic model requires adopting description of the FTO solid solution. The solid solution formed upon adding F to SnO_2 is modeled as a pseudobinary solid solution of SnF_2 and SnO_2, with a Gibbs energy of mixing obtained from regular-solution theory [1]. The gas phase is assumed as an ideal mixture of all its components.

a)   FTO Solid-Solution Phase

The FTO solid phase is described by a regular solution model whose Gibbs energy can be written as

$$G^{FTO} = {}^{ref}G^{FTO} + {}^{id}G^{FTO} + {}^{ex}G^{FTO}$$

with ${}^{ref}G^{FTO} = x_{SnO_2}G^0_{SnO_2} + x_{SnF_2}G^0_{SnF_2}$, ${}^{id}G^{FTO} = RT(x_{SnO_2}\ln x_{SnO_2} + x_{SnF_2}\ln x_{SnF_2})$, and where ${}^{ex}G^{FTO}$ is the excess Gibbs energy expressed by the regular solution model

$$^{ex}G^{FTO} = x_{SnO_2}x_{SnF_2}\Omega$$

where x_{SnO_2} and x_{SnF_2} are the mole fractions of the two end members, respectively SnO_2 and SnF_2, in the FTO solid solution phase. The symbols $G^0_{SnO_2}$ and $G^0_{SnF_2}$ represent respective the standard Gibbs energy of the pure SnO_2 and SnF_2 phases, and Ω is the regular-solution interaction energy parameter and is related to the energies of the bonds between SnO_2 and SnF_2. Positive values of Ω represent repulsive interactions, and negative values are associated with attractive interactions. The value of Ω is evaluated through the Delta Lattice Parameter (DLP) model as described in the next section.

b)   Gas Phase

Ideal mixing is often assumed, for the case of gases leading to quite reasonable description [1]. The Gibbs energy of the gas phase is then given by

$$G^{Gas} = {}^{ref}G^{Gas} + {}^{ideal}G^{Gas}_{mix}$$

with $G^{ref} = \sum_i x_i G_i^0$ and $G_{mix}^{ideal} = RT \sum_i x_i \ln x_i$, and where x_i is the mole fraction of component i

and G_i^0 defines the standard Gibbs energy of the phase containing the pure component i. The standard state of a substance is defined as its pure form in internal equilibrium under a pressure of 1 bar and at a given temperature. The number and type of components present in the gas phase are determined by experimental observation [9] [10].

4.2.2.2 Interaction Parameter Evaluation

The value of the interaction energy between SnO_2 and SnF_2 is estimated following an approach inspired on the standard Delta Lattice Parameter (DLP) methodology [3]. The standard DLP model [3] based on the dielectric theory of electronegativity of Philips and Van Vechten [4] suggests that the average band gap energy in compound semiconductor solutions that are primarily covalently bonded varies exponentially as a_0^n, where a_0 is the lattice constant. The enthalpy of atomization ΔH^{at} of either end member or of solid solution, which is related to bonding energy, is represented through the power law

$$\Delta H^{at} = K a_0^{\ n} \tag{4-1}$$

where *K and n* are empirical parameters obtained from experimental equilibrium data. The standard DLP model produces the fixed values of $K = 1.15 \times 10^4$ kcal/mol Å$^{-2.5}$ and $n = -2.5$ for cubic covalent systems. The components SnO_2 and SnF_2, however, are stable in the tetragonal structure. Thus new values for the power law exponential constant n and proportionality constant K must be estimated for the Group IV tetragonal oxide semiconductors. This can be achieved by making use of available covalent bonding energy and lattice parameter data. The tetragonal oxides SiO_2, GeO_2, SnO_2 and PbO_2 are chosen because they belong to the same space group, namely, $P4_2/mnm$ [2]. The original DLP model considered only one lattice parameter because it was developed for cubic systems. In our approach for tetragonal systems, the lattice constant a_0 is used for estimating the exponential parameter n and proportionality parameter K. Selecting the a_0 value is supported by the observation that this particular lattice parameter changes significantly in CVD-grown $Sn(O_xF_{1-x})_2$ films, as shown in Table 4-1. This table shows values of the lattice constants measured by XRD for both pure SnO_2 and for fluorine-doped films SnO_2:F. Note that the value of the a_0 parameter changes by 0.68% while the c_0 parameter changes by only 0.09%. As a first step to estimate the interaction energy, the enthalpy of atomization of each compound is needed.

The enthalpy of atomization of a compound is the enthalpy change associated with breaking apart the compound to its gaseous atoms at 298 K and 1 atm. The enthalpy of atomization gives directly the sum of the contributing bond enthalpies for a gaseous compound, but for solids and liquids additional enthalpy terms are included in H^{at}, reflecting intermolecular and interionic interactions. Thus for the general compound AB_2, the atomization process is:

$$AB_2 \rightarrow A(g) + 2B(g)$$
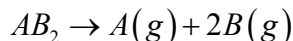
The corresponding enthalpy of atomization of a compound is:

$$\Delta H^{at} = -\Delta H_f^0 + H^{at}(A) + 2H^{at}(B_2)$$

where ΔH_f^0 is the enthalpy of formation of AB₂ A from solid and B₂ gas, $H^{at}(A)$, and $H^{at}(B_2)$ are respectively the atomization enthalpies for solid A and gas B₂. The values of ΔH_f^0 are taken from the JANAF compilation [6]. Values for the latter three enthalpies are available in the literature [5]. Table 2 summarizes the calculated values of atomization enthalpies as well as the lattice constants for tetragonal compounds of interest. The left most column lists the five tetragonal compounds. The enthalpy of atomization of the pure covalent bond is listed in the second column. The third column is the enthalpy of atomization when the ionicity of the bond is taken into consideration. The ensuing columns show the lattice constant a_0 and c_0. Note that the lattice constant a_0 reported for SnF₂ in Table 4-2 is for the pure compound.

A regular solution interaction parameter, Ω, can now be calculated by assuming that the mixing enthalpy ΔH^M follows the regular solution form

$$\Delta H^M(x) = \Omega\, x(1-x) \tag{4-2}$$

where x is the fractional composition of the end member SnF₂. The composition dependence of ΔH^M is given by the relation

$$\Delta H^M = (1-x)\Delta H^{at}_{SnO_2} + x\Delta H^{at}_{SnF_2} - \Delta H^{at}_{alloy} \tag{4-3}$$

where $\Delta H^{at}_{SnO_2}$ is the atomization energy of SnO₂, $\Delta H^{at}_{SnF_2}$ is the atomization energy of SnF₂, and ΔH^{at}_{alloy} is the atomization energy for the alloy (solid solution) formed by SnO₂ and SnF₂. Now, after setting $x = 0.5$, equations (4-2) and (4-3) can be combined with equation (4-1) and solved for the interaction parameter to obtain

$$\Omega = 4K\left\{ -\left(\frac{a_{SnO_2} + a_{SnF_2}}{2}\right)^n + \frac{1}{2}(a^n_{SnO_2} + a^n_{SnF_2}) \right\} \tag{4-4}$$

In the following subsection a), an estimate of Ω is carried out assuming that the lattice constants appearing in equation (4-4) are interpreted as the corresponding lattice parameter a_0 in the tetragonal sublattice.

a)   Power law model based on lattice constant a_0

Figure 4-1 shows a plot of the atomization energy versus the crystal's lattice constant a_0. The diagonal markers denote the atomization energy values for the oxides reported in Table 4-2 for the case of covalent bonds. The square markers denote the respective oxide energies for the case where the ionicity of the bonds is also taken into account. The continuous curve shown in the figure represents the plot of a least-squares fit of the power law given in equation (4-1) to the covalent bond data, yielding the model

$$\Delta H^{at} = 4.3906 \times 10^4 a_0^{-3.2271} \text{ kcal/mol (Covalent)} \tag{4-5}$$

Finally, the dashed line represents the least-squares fit to the data that involves ionic effects through the model

$$\Delta H^{at} = 7.215 \times 10^4 a_0^{-3.377} \text{ kcal/mol (Covalent+Ionic)} \tag{4-6}$$

Selecting $K = 4.3906 \times 10^4$ kcal/mol and $n = -3.2271$ from equation (4-5) and substituting these values into equation (4-4) yields the value of the interaction parameter $\Omega = 8.52$ kcal/mol for the case of covalent bonding. Proceeding analogously, adopting the parameters indicated in equation (4-6) yields the valued $\Omega = 11.71$ kcal/mol when taking the ionicity of the bond into consideration

The gas phase is generally at a relatively low pressure and at elevated temperature near the substrate surface. Chemical compositions in equilibrium with the solid solution were calculated using the ThermoCalc software tool [1] which requires input of the interaction parameter to compile a database of Gibbs energy for each phase involved in the equilibrium.

b) Validation of the approach

In order to validate the results obtained via the DLP method, we calculate the interaction parameter for $SiO_2 - GeO_2$ based on the power law relationship (5) and compare the value with that obtained from the phase diagram [7]. The results are listed in Table 4-3, where it can be seen that the reported values are close to each other. This closeness of the results suggests that the proposed DLP approach is consistent with phase-diagram data.

All the ensuing calculation in this paper are based on the interaction parameter value $\Omega = 8.52$ kcal/mol. Calculations based on other interaction-parameter values show a similar trend, except for a slight F solubility difference.

4.2.2.3 F Solubility Limit Expression

The solubility of F in SnO_2 is limited and similarly the solubility of O in SnF_2 is limited. In this section, it is argued that the temperature dependence of the solid solubility x of SnF_2 in SnO_2 can be written as

$$x = \exp(-\Omega / RT) \tag{4-7}$$

The rest of this section presents a detailed derivation of equation (4-7).

At the solubility limit, fluorine-saturated SnO_2 is in equilibrium with oxygen-saturated SnF_2. The solubility limit is calculated by equating the chemical potential of SnF_2 in the two solid phases [8]

$$\mu_{SnF_2}{}^{(I)} = \mu_{SnF_2}{}^{(II)} \tag{4-8}$$

where the superscripts I and II represent the SnO_2- and SnF_2-rich solid phases respectively and μ is the chemical potential. Since $\mu_i = \mu_i^0 + RT \ln \bar{a}_i$ and the standard state μ_i^0 is the same for both phases, equation (4-8) implies that

$$\bar{a}_{SnF_2}{}^{(I)} = \bar{a}_{SnF_2}{}^{(II)} \tag{4-9}$$

where μ_i and μ_i^0 are the chemical potential and the standard chemical potential for species i, and $\bar{a}_i$ is the activity of the component i in the solution.

We assume that the SnO_2-rich phase is composed of a nearly pure SnO_2, hence

$$\bar{a}_{SnF_2}{}^{(I)} = 1 \tag{4-10}$$

Also, the activity expression for the SnF_2-rich phase is given by [1]

$$\bar{a}_{SnF_2}{}^{(II)} = x \exp(\bar{G}_{SnF_2}{}^{xs} / RT) \tag{4-11}$$

where $\bar{G}_{SnF_2}{}^{xs}$ is the partial molar excess free energy of SnF_2 in SnO_2. The excess free energy G^{xs} of the solid solution is $G^{xs} = \Delta H^M - T\Delta S^{M,xs}$, where ΔH^M is the enthalpy of mixing and $\Delta S^{M,xs}$ is the excess entropy of mixing. It is assumed that the solid solution between SnO_2-SnF_2 can be described by a regular solution model;

$$G^{XS} = \Delta H^M = \Omega_{SnF_2 - SnO_2} x_{SnF_2} \left(1 - x_{SnF_2}\right) \tag{4-12}$$

Then

$$\bar{G}_{SnF_2}{}^{xs} \equiv \left.\frac{\partial(N_0 \Delta H^M)}{\partial N_{SnF_2}}\right|_{N_{SnF_2}=0} = \left.\frac{d\Delta H^M}{dx_{SnF_2}}\right|_{x=0} \tag{4-13}$$

where N_0 is the total moles of SnF_2 and SnO_2. Substituting equation (4-12) into equation (4-13) yields

$$\bar{G}_{SnF_2}{}^{xs} = \left.\frac{d\Delta H^M}{dx_{SnF_2}}\right|_{x=0} = (1 - 2x_{SnF_2})\Omega_{SnF_2 - SnO_2}\Big|_{x=0} = \Omega_{SnF_2 - SnO_2} \tag{4-14}$$

which is the partial molar enthalpy of mixing at infinite dilution. Finally, substituting equations (4-9), (4-11), and (4-14) into the activity equality (4-10) and solving for the fluorine solubility x yields the relationship (4-7).

4.2.2.4 CVD Mechanism

The mechanism of the chemical vapor deposition of SnO_2 from tetramethyltin and oxygen is complex. Borman *et al.* [9] studied the gaseous reaction by-products by gas chromatography and mass spectrometry. They found that virtually all the TMT reacted and that only 0.1% of the CF_3Br reacted at the growth conditions 743K, 0.1% TMT, 3.95% CF_3Br, and 20% O_2. The dominant species observed in the reactor effluent were H_2CO, H_2O, HF, CO, CO_2, CH_4, and CH_3Br. In addition to these, HBr, C_2H_6, C_2H_4, CF_3H, C_2H_2, CF_2CH_2 also exists in a ppm scale. Li *et al.* [10] found that the presence of CH_4 can increase the conversion level of $CBrF_3$. Furthermore, the species CHF_3, CH_3Br, $C_2H_2F_2$, C_2H_2, $C_2H_3F_3$, C_2HBrF_2, C_2H_3F, C_2HF_5, C_2F, C_6H_5F, $CHBrF_2$, C_2H_3Br were found to be the main gas by-products [10]. Therefore, the following mechanism for CVD formation of FTO is suggested:

Based on the available evidence, it is possible to propose a mechanism for the CVD formation of FTO. First, TMT is completely decomposed at the substrate surface by the reaction:

$$Sn(CH_3)_4 \rightarrow Sn + CH_3^{\bullet}$$
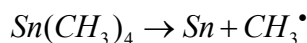
and tin is oxidized through the reaction:

$$Sn + O_2 \rightarrow SnO_2$$
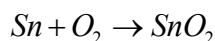
Then, some of the CH_3 material is oxidized to CO_2 and H_2O, and the residual CH_3 participates in enhancing the pyrolysis of $CBrF_3$ and produce the gas by-products mentioned in the previous paragraph.

To better understand the growth chemistry, a chemical equilibrium calculation was performed assuming that the growing vapor-solid interface is at equilibrium. The calculation is carried out within the temperature range of 400 ~ 900 K because above 900 K a carbonaceous deposit was observed on the surface of thermocouple sheaths resulting in the decrease of carbon mass balance [10]. The results of the calculation are presented in Section 4.2.3.2.

4.3 Results and Discussion

4.3.1 Solid Solubility Limit of F in Various TCO Materials

The oxides SnO_2, CdO, ZnO, and In_2O_3 are the most commonly used TCO materials. The F doping solubility limit in these materials is estimated by using DLP model given in equation (4-12), and the results are shown in Figure 4-2. Note that in these oxides, the greatest F solubility observed is in the SnO_2 material, which is consistent with the experimental observation that the F solubility in SnO_2 is higher than that in ZnO [12]. There is great interest in CdO because of its high electron mobility, and because undoped CdO can produce a carrier concentration up to 1×10^{21} cm^{-3}. The doped CdO materials listed experimentally in [13] show insignificant variation in carrier concentration, indicating that F has a low solubility in CdO, a fact that is consistent with the results of Figure 4-2. The bottom-most curve on Figure 4-2 shows

the solubility of fluorine in In_2O_3 which is a prediction that can be of utility given that there is insufficient literature data for this material.

4.3.2   Analysis of FTO growth via CVD

Figure 4-3 shows the chemical equilibrium conversion level of F in a CVD system for the three different precursors as a function of temperature. The conversion level is defined as the ratio of the amount of decomposed precursor to the initial precursor input in the gas phase. The calculation were made assuming the mechanism and the gas species proposed in section 4.2.2.4, and utilizing the Thermo-Calc software package [1]. The data given in the figure show that ClF_3 decomposes more than $CBrF_3$, which in turn decomposes to a greater extent than CF_4. Figure 4-4 plots the equilibrium F concentration in the FTO solid-solution phase versus temperature for different precursors. The extent of the equilibrium F concentration in solid phase follows the sequence: $ClF_3>CBrF_3>>CF_4$ as shown in Figure 4-4. Therefore, the first two are the preferred precursors. This is consistent with experimental observations [11].

Figure 4-5 shows the conversion level of the $CBrF_3$ as a function of initial $CBrF_3$ inlet component at different temperature. For all temperature considered, the conversion level is always higher at low initial $CBrF_3$ concentrations. It is relevant to note that the conversion is low at the growth temperature of 773 K typically used for CVD growth, independent of the initial $CBrF_3$ mole concentration. More specifically, at 773 K and at initial CBrF3 mole fraction of 0.04 only 0.6% of $CBrF_3$ decomposes according to the calculation, which is consistent with the experimentally reported decomposition of 0.1 % at 1 atm [9].

Figure 4-6 compares the calculated atomic concentration of F in FTO with the experimentally-measured F secondary ion counts and measured carrier concentration. The results are plotted as a function of $CBrF_3$ partial pressure. The triangle markers are the measured ion F counts measured by SIMS and the square markers are the experimental carrier concentration data points by Hall measurements. The dahsed line without any markers is the calculated F concentration in the FTO film. As can be seen, the calculated and experimental trends are similar, that is, both the F and carrier concentrations increase rapidly as the $CBrF_3$ initial mole fraction increases. Note also that the carrier concentration increases as the F atomic concentration increases, and eventually saturates for large $CBrF_3$ inlet compositions. The F concentration (dashed line) is much larger than carrier concentration (square marker); this is explained by the fact that the F is not totally ionized. At other temperatures, as shown in Figure 4-7, the F concentration follows the same trend as described above except that there is a higher F concentration at higher temperature.

Figure 4-8 shows the F concentration in FTO film as a function of growth temperature. The top dashed is the calculated solubility limit. The bottom solid line is the calculated F concentration which increases with temperature since more F precursor decomposition occurs. However, in the actual CVD experiments, the $CBrF_3$ sticking coefficient decreases as the temperature increases; therefore, the experimental F concentration may be observed to decrease with the temperature.

4.3.3   Conclusions

The F concentration in F doped SnO_2 (FTO) film was estimated as a function of the growth

temperature and the dopant precursor inlet composition using an equilibrium model. The effect of different dopant precursors (CF_4, $CBrF_3$, and CIF_3) on F concentration in FTO was also calculated and compared with experimental results [11]. It is found that $CBrF_3$ is very reactive, although as not reactive as CIF_3. The reactivity of CF_4 is much lower than the other two precursors.
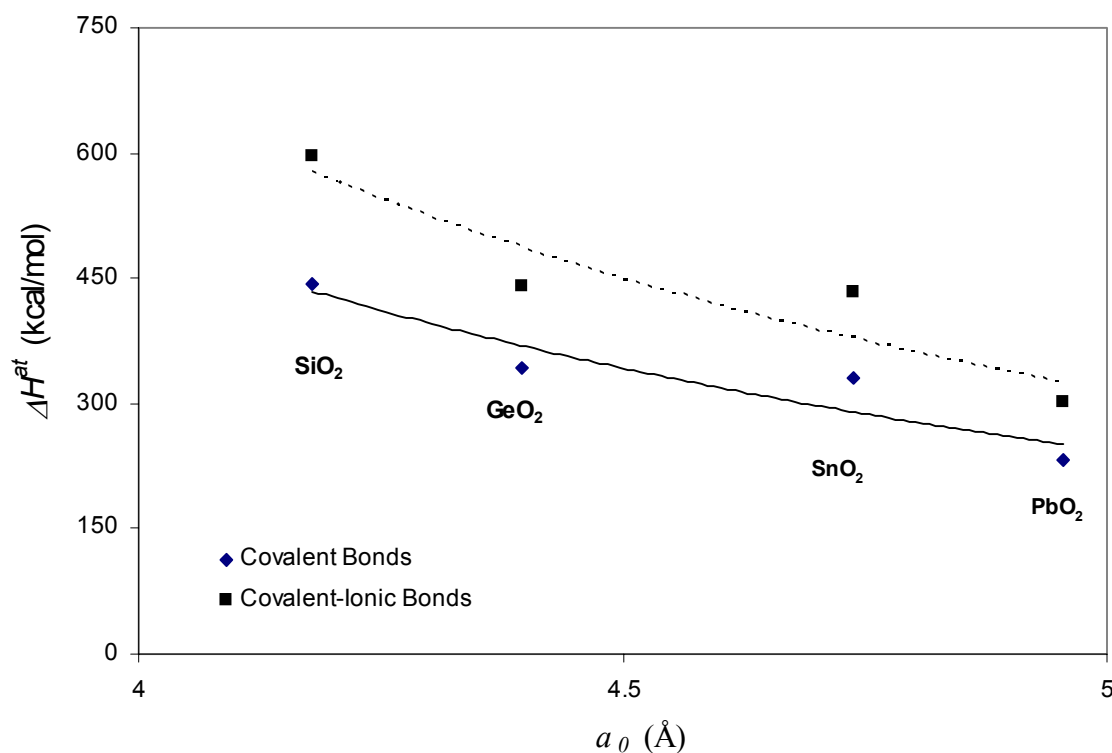

Figure 4-1. Power law relationship relating the heats of atomization and lattice constant a_0 for oxides of interest under the assumption of covalent-only bonds and covalent plus ionic bonds.
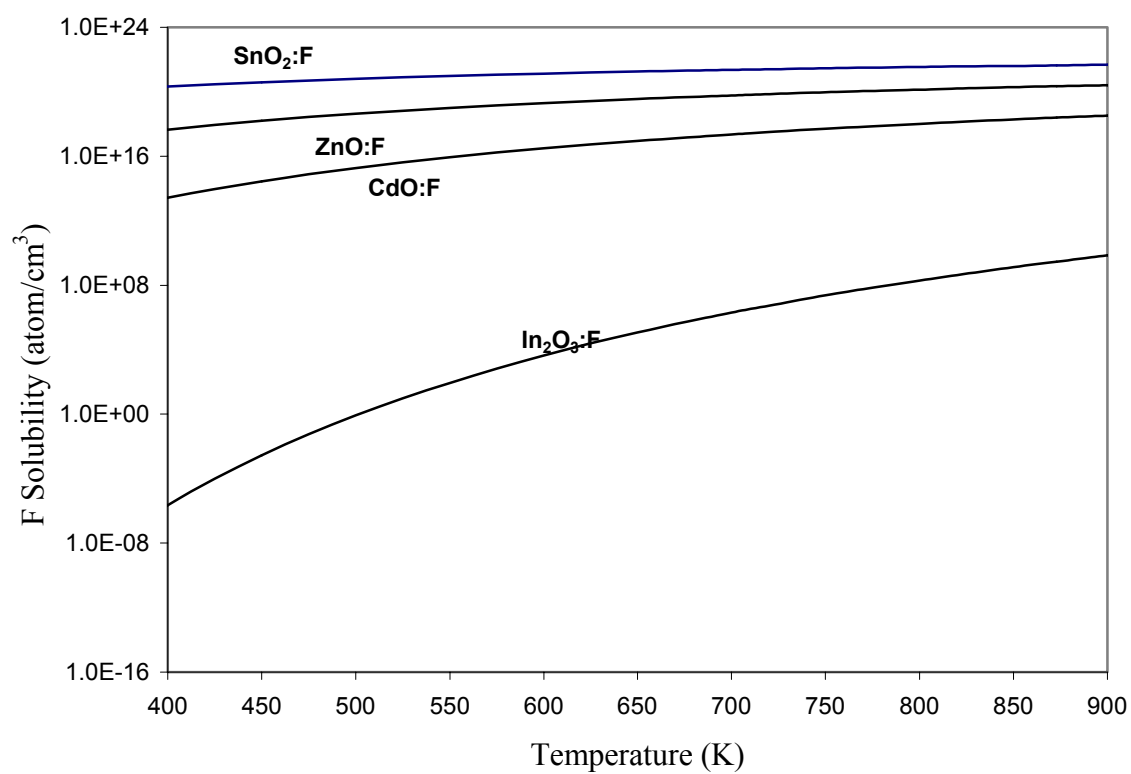
Figure 4-2. Solid solubility limit of fluorine in different TCO materials versus temperature calculated using the DLP model.
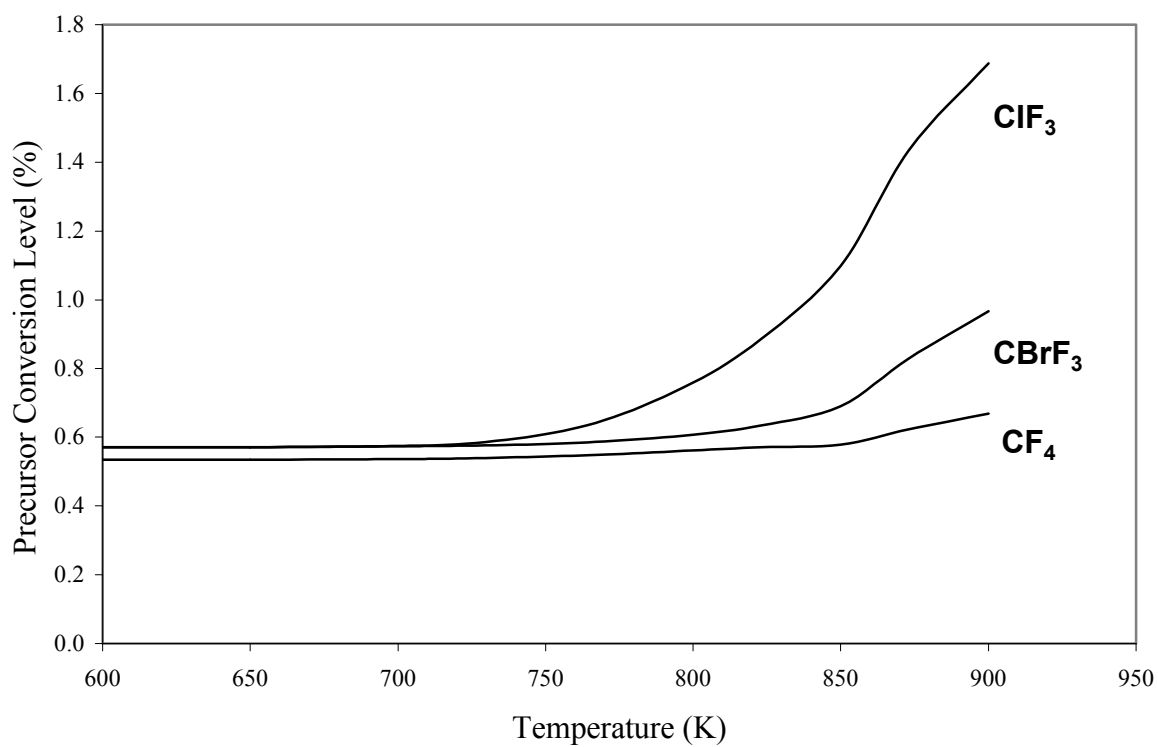
Figure 4-3. Calculated conversion level of three different fluorine-containing precursors as a function temperature. CVD conditions: 18.96 mol% $CBrF_3$, 44.43 mol% O_2, 0.592 mol% TMT, 36.02 mol% N_2 and P=40 Torr.
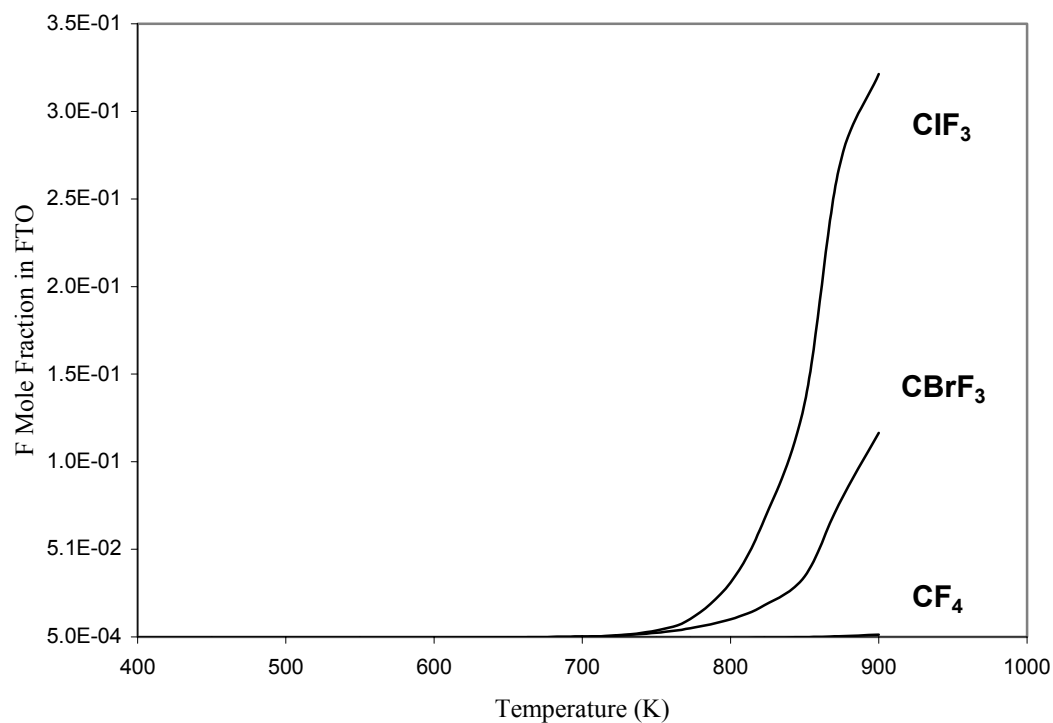
Figure 4-4. Calculated equilibrium fluorine concentration in FTO of three different fluorine-containing precursors as a function temperature. CVD conditions: 18.96 mol% $CBrF_3$, 44.43 mol% O_2, 0.592 mol% TMT, 36.02 mol% N_2 and P=40 Torr.
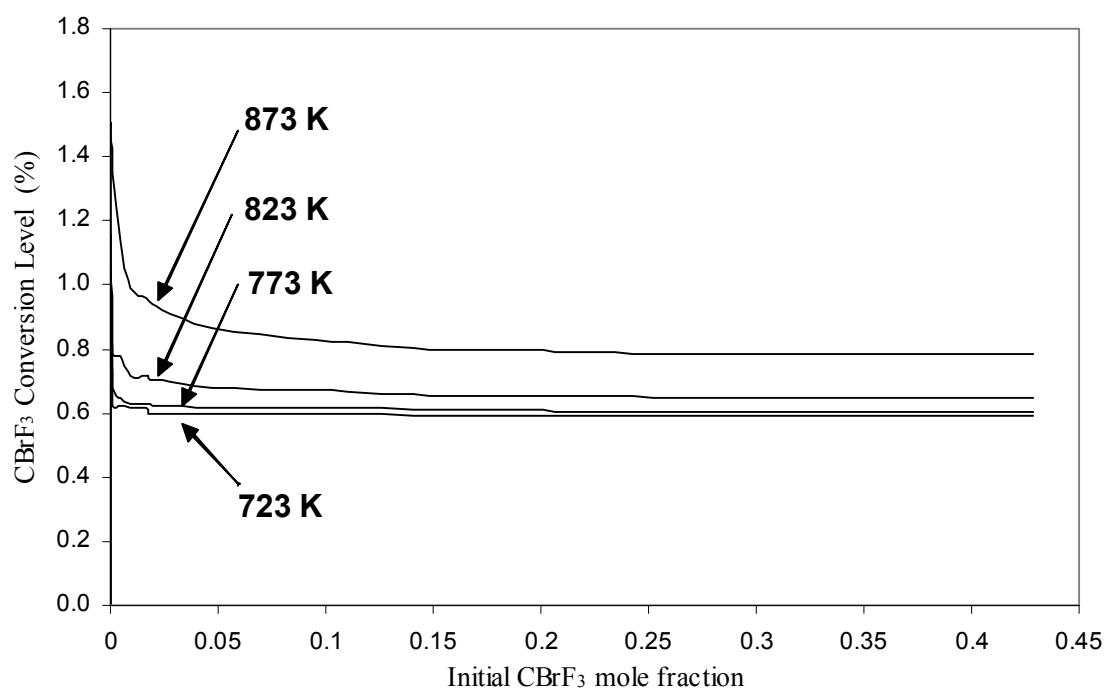
Figure 4-5. Calculated $CBrF_3$ conversion level versus initial $CBrF_3$ mole fraction at different temperature at initial mole concentration. CVD conditions: 44.43 mol% O_2, 0.592 mol% TMT and total pressure of 40 Torr.
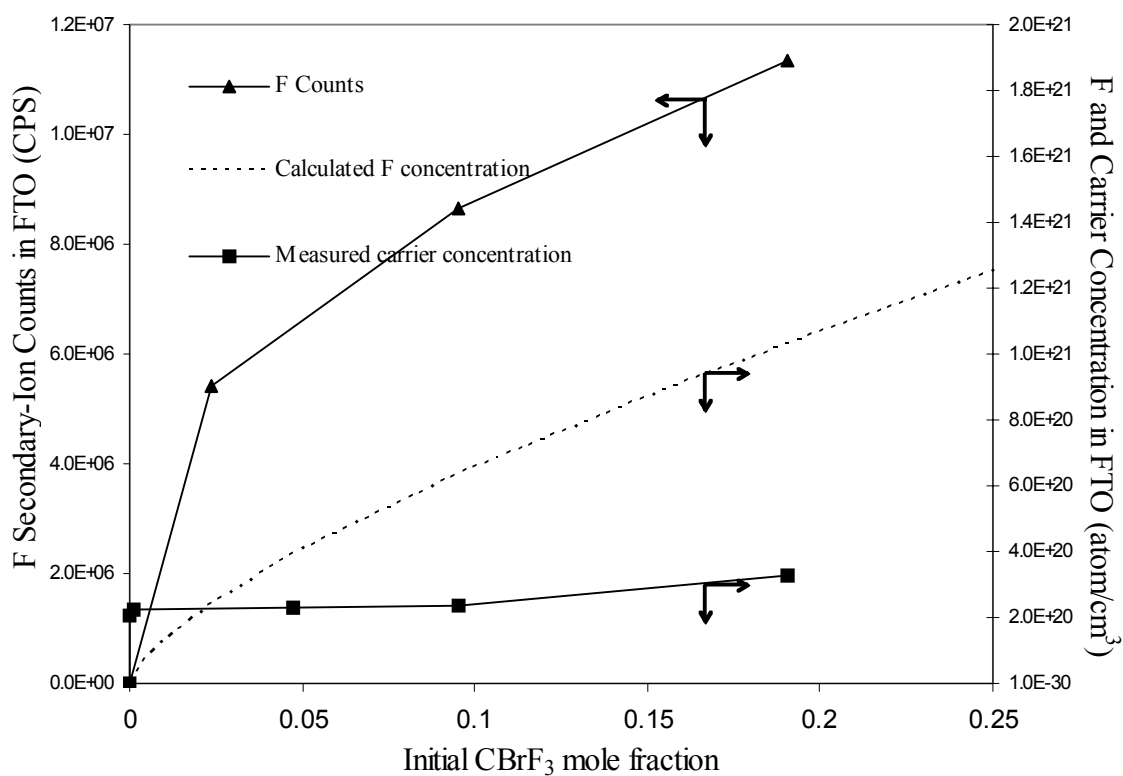
Figure 4-6. Comparison of F concentration in FTO versus initial CBrF$_3$ mole fraction by calculation, Hall measurement and SIMS analysis at fixed T$_s$= 550 °C, 44.43% O$_2$, 0.592% TMT and total pressure 40 Torr.
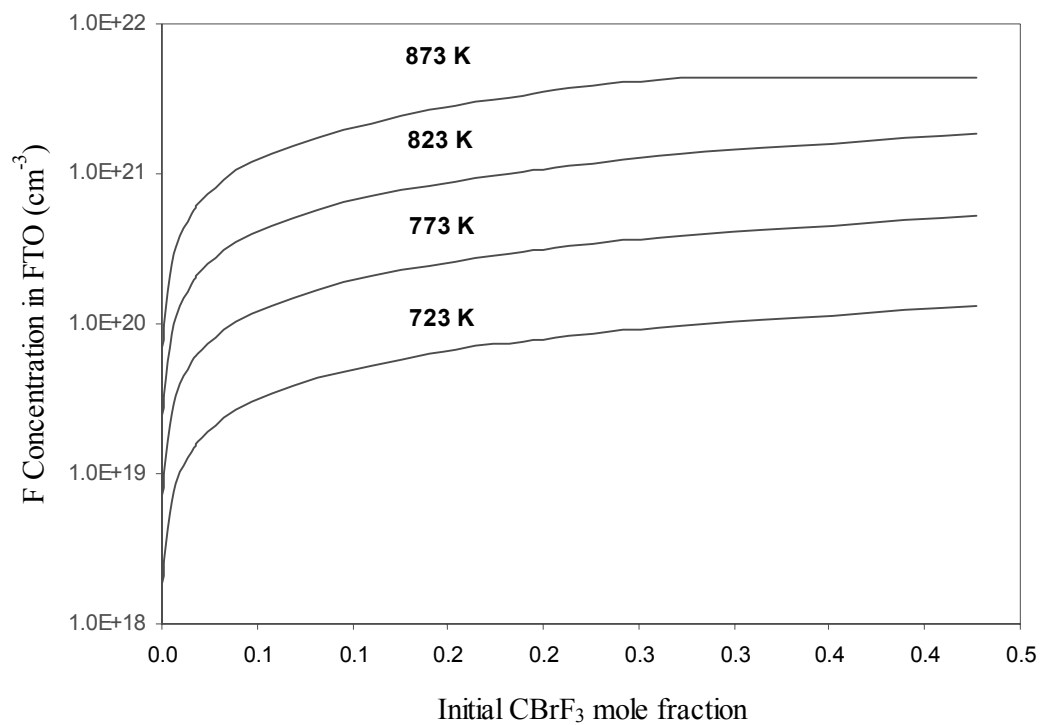
Figure 4-7. Calculated F concentration at different temperature as a function flow rate. CVD conditions: 44.43 mol% O_2, 0.592 mol% TMT and total pressure of 40 Torr .
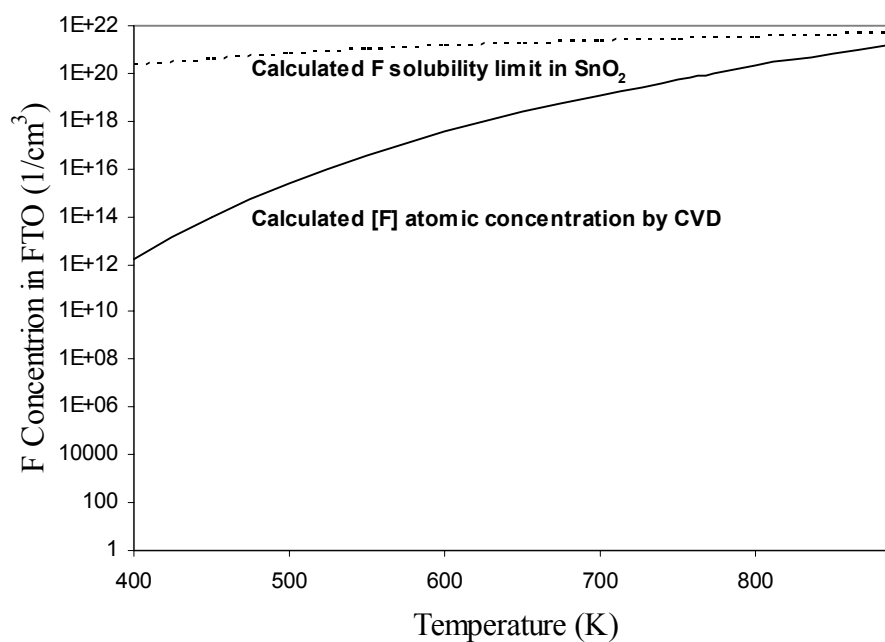
Figure 4-8. Comparison of F Incorporation and solubility limit as a function of temperature. CVD conditions 18.96 mol% $CBrF_3$, 44.43 mol% O_2, 0.592 mol% TMT, 36.02 mol% N_2 and P=40 Torr.

Table 4-1. Experimental lattice constant values and composition of FTO films grown by CVD.

	a_0 (Å)	c_0 (Å)
SnO₂	4.740	3.177
SnO₂:F	4.772	3.174

Table 4-2. Atomization enthalpy and lattice constants for selected tetragonal compounds.

Material	Enthalpy of Atomization (Covalent Bond) ΔH^{at} (kcal/mol)	Enthalpy of Atomization (Covalent+Ionic Bond) ΔH^{at} (kcal/mol)	Lattice Constant a_0 (Å)	Lattice Constant c_0 (Å)
SiO_2	443.8	596.96	4.179	2.6649
GeO_2	341.9	441.51	4.3963	2.8626
SnO_2	330.1	434.12	4.738	3.187
PbO_2	233.3	302.19	4.9564	3.3877
SnF_2	265.0	441.32	5.0733	8.491

Table 4-3. Comparison of calculated Ω for SiO_2-GeO_2 based on DLP and experimental Ω obtained from phase diagram data.

	Ω From DLP (kcal / mol)	Ω From $T_c = \Omega/2R$ (kcal / mol)
$SiO_2 - GeO_2$	a_0	
	7.11	6.67 [7]

4.4 Publications and presentations

1. L. L Kerr, X. Li, T. J. Anderson, R. Noufi, T. Coutts, O.D. Crisalle, and S. Li "Thermodynamic Modeling of F doping in SnO2", published in the 30th World Photovoltaic Specialist Conference Proceedings, Japan (2003).

2. L. L. Kerr, S.S. Li, S. W. Johnston, T. J. Anderson, O.D. Crisalle, and R. N. Noufi " Deep Level Transient Spectorscopy (DLTS) Characterization of Team CIGS Cells", *published in the 20th NCPV Photovoltaics Program Review Proceedings*, Golden, CO (2003).

4.5 References cited

[1]   N. Saunders and A.P. Miodownir, *CALPHAD – Calculation of Phase Diagram*, Oxford, New York, Pergamon, 1998.

[2]   P.Villars and L.D. Calvert, *Peasrson's Handbook of Crystallographic Data for Intermetallic Phases,* Metals Park, OH, American Society for Metals, 1985.

[3]   G.B. Stringfellow, *Orgnaometallic Vapor-Phase Epitaxy*, Academic Press Inc. 1989.

[4]   J.A. Van Vechten, "Quantum Dielectric Theory of Electronegativity in Covalent Systems. II. Ionization Potential and Interband Transition Energies", Physical *Review*, Vol. 187, No.3, pp.1007-1020, 1969.

[5]   *Handbook of the Physicochemical Properties of the Elements*, Plenum: New York, 1968.

[6]   *JANAF Thermochemical Tables*, Washington, D.C.: American Chemical Society, New York: American Institute of Physics for the National Bureau of Standards, 1986.

[7]   G. Baret, R. Madar, and C. Bernard, "Silica-Based Oxide Systems", *J. of Electrochem. Soc,* Vol. 138, No. 9 pp. 2831-2835, 1991.

[8]   G.B. Stringfellow, "Calculation of the Solubility and Solid-Gas Distribution Coefficient of N in GaP", *J. of Electrochem. Soc,* Vol. 119, No.12 pp. 1780-1782, 1972.

[9]   C.G. Borman, and R. Gordon, "Reactive Pathways in the Chemical Vapor Deposition of Tin Oxide Films by Tetramethyltin Oxidation", *J. Electrochem. Soc.*, Vol. 136, No. 12 pp. 3820-3828, 1989.

[10]   K. Li, E. M. Kennedy, and B.Z. Dlugogorski "Experimental and Computational studies of the pyrolysis of $CBrF_3$, and the reaction of $CBrF_3$ with CH_4", *Chemical Engineering Science*, Vol. 55, pp 4067-4078, 2000.

[11]   R. Gordon, "Method of depositing electrically conductive, infra-red reflective, transparent coatings of stannic oxide", *United States Patent* 4146657 Mar 27, 1979.

[12]   J. Hu and R. Gordon, " Electrical and optical properties of doped tin and zinc oxide thin films by atmospheric pressure chemical vapor deposition", *American Institute of*

Physics, pp. 381-387, (1992).

[13]   X. Li, T. Barnes, C. DeHart, D. King, S. Asher, M. Young, T.A. Gessert, and T.J. Coutts, "Doping Effects on CdO Thin Films", *Mat. Res. Soc. Symp. Proc*. Vol. 666, pp. F3.18.1-F3.18.6, 2001.

5   XAFS Studies

Participants: Alex Chang (Faculty Advisor), Giang N. Ma (Graduate Research Assistants).

5.1 Objectives

Synthesize and characterize CIS and CIGS samples of selected compositions in the solid solutions of $Cu(_{In1-x}Ga_x)Se_2$, $Cu(_{In1-x}Ga_x)_3Se_5$ and Cd treated CIGS samples by XAFS and XPS measurements.

5.2 Accomplishments

The *ab initio* multiple-scattering code FEFF8 was used to provide additional quantitative details about the local environment of Cd in the $CuInSe_2$ 1852 sample treated with a 1.5 M concentration of cadmium salt (which is denoted CIS:Cd). Specifically, the amount of Cd-O and Cd-Se interactions within the CIS:Cd sample will be determined.

There is trong evidence of Cd-Se, Cd-O and/or Cd-OH bonds found in Cd-k edge data for CIS:Cd samples. These interfacial bonds may play an important role in the efficiency of solar cell devices. We have analyzed these materials by WinXAS using FEFF8-calculated phase shifts and scattering amplitude functions.

The first model considered incorporated both cadmium and oxygen atoms into the CIS:Cd lattice. Specifically, an oxygen atom is introduced in the tetrahedral bonded Cd-Se structure. Figure 5-1 shows a crystallographic structure of this one-phase model. The atom identification is done as follows: Copper atoms are represented small grey balls, Indium atoms as large black balls, Selenium atoms are large light-grey balls, Cadmium atoms are large gray balls, and finally, the Oxygen atom is given as the large white ball. The main peak observed in the data represents the Cd-Se bonds, which match well standard fits with a coordination number of 2.54 atoms at a distance of 2.63 Å apart. The fit also suggested that the Cd has 3.48 O as its nearest neighbors in addition to the Se nearest-neighbors. Key results obtained are tabulated in Table 5-1. This analysis suggests that the samples studies do not contain Cd(O,Se) tetrahedrons.
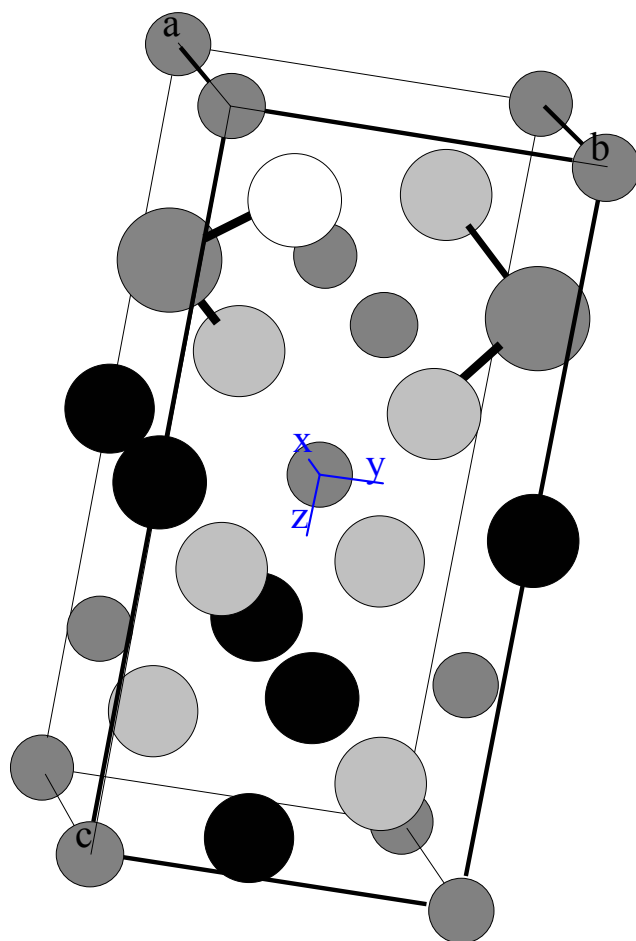
Figure 5-1. Crystal structure of the one phase model containing the tetrahedrally bonded cadmium atom (Shown as large gray balls with darkened bonds).

Table 5-1: Least square fitting results of the one phase model in CIS:Cd.

	Coordination Number	**Bond Length (Å)**	**$\sigma^2(\text{Å}^2)$:**	**S_0^2:**
Cd-K edge	2.54	R_{Cd-O} 2.28	$1.24\text{X}10^{-2}$	0.94
	3.48	R_{Cd-Se} 2.63	$7.88\text{X}10^{-3}$	0.94

Current efforts focus on data analysis based new models.

5.3 Publications and presentations

[1]   G.N. Ma, C.-H. Chang, S.Yoon, T.J. Anderson, Rommel Noufi, Report No. B4.4, "XAFS Investigations of the Local Structure of Cadmium in $CuInSe_2$-Based Materials", *Materials Research Society Spring Meeting: Symposium B Compound Semiconductor Photovoltaics*, San Francisco, CA, 2003.

[2]   G.N. Ma, C.-H. Chang, S. Yoon, T.J. Anderson, Rommel Noufi, Graduate Student Poster, "XAFS Investigations of the Local Structure of Cadmium in $CuInSe_2$-Based Materials", *14th Annual Symposium of the Pacific Northwest Chapter of the American Vacuum Society*, Troutdale, OR, 2003.

6   Thermodynamic Assessment of the Cu-Ga-In Ternary System

Participants: Timothy J. Anderson (Faculty Advisor), and Woo Kyoung Kim (Graduate Research Assistant).

6.1 Objective

Assess the phase diagram and thermochemical properties of Cu-Ga-In ternary system.

6.2 Accomplishments

6.2.1   Ternary phase diagram prediction from three sub-binary systems

Our research group has been employing the ThermoCalc software to perform rigorous assessments of the binary or ternary subsystems in the $Cu(Ga_xIn_{1-x})Se$ system. As a first step in using the Thermocalc program to estimate the Cu-Ga-In ternary phase diagram, we prepared the ternary Thermodynamic DataBase (TDB) module which contains the Gibbs energy information of pure Cu, Ga, and In elements as well as the interaction parameters of three sub-binary Cu-Ga [1], Cu-In [2] and Ga-In [3] systems.

There were no experimental reports in the literature on ternary interaction parameters for the Cu-Ga-In system. Therefore, the Muggianu's geometric mixing model, which is widely applied to metallic systems, was employed to extrapolate the binary excess Gibbs energy of mixing into the ternary melt [4].

$$G_{mix}^{xs} = x_A x_B \left\{ L_{AB}^0 + L_{AB}^1 (x_A - x_B) \right\} + x_B x_C \left\{ L_{BC}^0 + L_{BC}^1 (x_B - x_C) \right\} + x_A x_C \left\{ L_{AC}^0 + L_{AC}^1 (x_A - x_C) \right\} \qquad (6\text{-}1)$$

where L^0 is the binary interaction parameter of the regular solution model and L^1 is the binary interaction parameter of the sub-regular solution model.

Based on the Muggianu's model, the ternary phase diagrams of the Cu-Ga-In system were predicted using ThermoCalc, as shown in Figures 6-1 and 2. These phase diagrams are the isothermal sections at 500 and 350°C, respectively. In these phase diagrams, five different solid solution phases and a liquid phase region were included.

The diagrams presented in Figures 6-1 and 2 were estimated on the basis of binary information only, that the models do not contain any ternary interaction parameters. To obtain a more reliable ternary phase diagram, ternary interaction parameters should be added to the liquid solution Gibbs energy model of ternary Cu-Ga-In system in the form $G_{ABC} = x_A x_B x_C (L_A x_A + L_B x_B + L_C x_C)$. As part of our program, ElectroMotive Force (EMF) measurement will be employed to measure the activity of Ga and the formation Gibbs energy of Cu-Ga-In ternary compounds. The preliminary ternary phase diagram predicted using the Muggianu's model will be helpful to design the EMF experiments. The ternary interaction parameters will be assessed using the EMF experimental data and the thermo-optimization module in ThermoCalc.
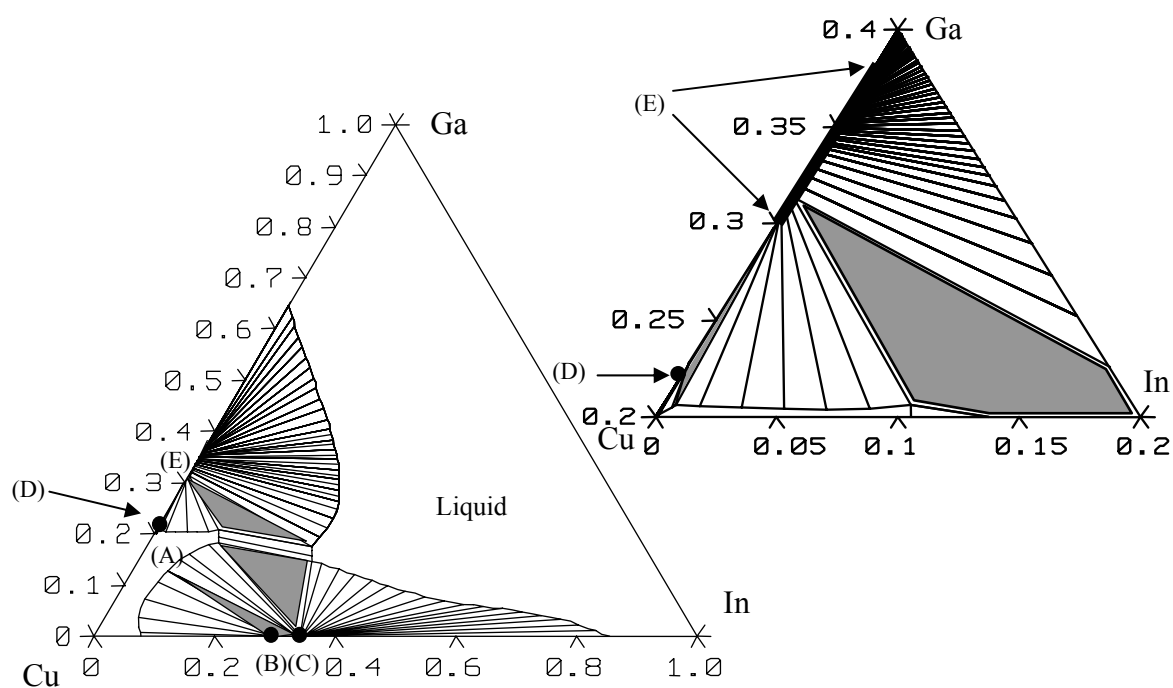
Figure 6-1. Isothermal section(500°C, 1atm) of Cu-Ga-In ternary Phase Diagram based on Muggianu's equation. (A) α-Cu_FCC (B) δ-Cu$_7$In$_3$ (C) η-Cu$_2$In (D) ξ-CuGa solid solution (E) γ-CuGa solid solution.
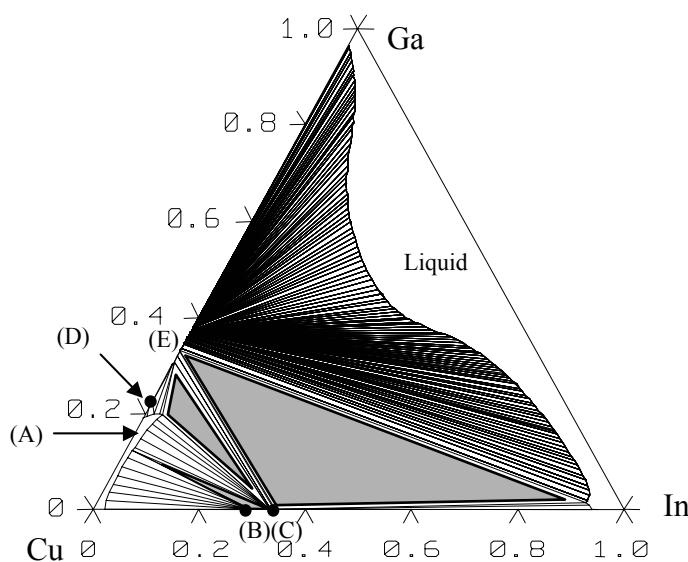

Figure 6-2. Isothermal section(350°C, 1atm) of Cu-Ga-In ternary phase diagram based on Muggianu's equation.

6.2.2   Vapor pressure assessment of Cu-Ga-In system

To help design the ElectroMotive Force (EMF) experiments, the vapor pressure was estimated at various T and compositions in this ternary system. The vapor pressures for Cu-Ga-

In mixtures at several compositions were calculated using the ThermoCalc software package in combination with the Cu-Ga-In ternary Thermodynamic DataBase (TDB) module. Selected results are shown in Figure 1-3(Cu:Ga:In = 1:1:1) and Figure 1-4(Cu:Ga:In = 2:1:1).

According to the vapor pressure calculations, six vapor phase species dominate the gas phase: Cu, Cu_2, Ga, Ga_2, In and In_2. Among them, atomic indium (In) is the most volatile phase.
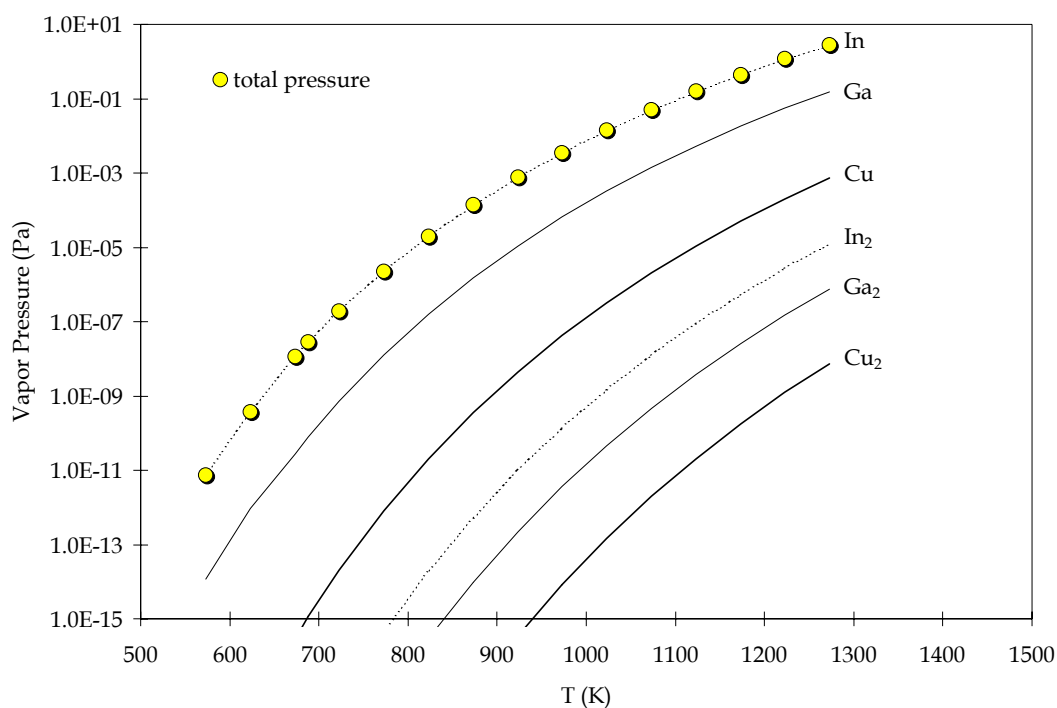

Figure 6-3.   Vapor pressure as a function of temperature in the Cu-Ga-In mixture (Cu:Ga:In = 1:1:1 mole ratio).
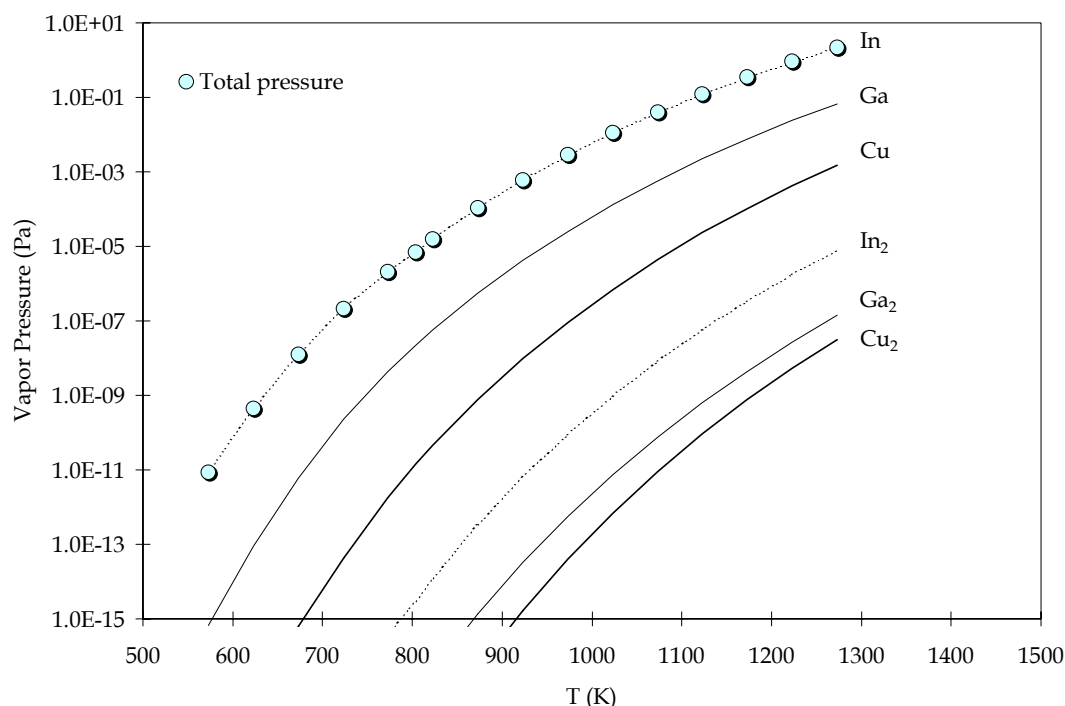
Figure 6-4.   Vapor pressure as a function of temperature in the Cu-Ga-In mixture (Cu:Ga:In = 2:1:1 mole ratio).

6.3   References cited

[1]   P. R. Subramanian, T. B. Massalski and D. E. Laughlin, " Thermodynamic Aspects of Massive Transformations in The Cu-Ga and Cu-Zn Systems", *Acta metail*, 36(4), pp.937 (1988).

[2]   C.R. Kao, A. Bolcavage, S.–L. Chen, S.W. Chen, Y.A. Chang, and A.D. Romig, Jr., "Phase Equilibria of the Cu-In System- I: Thermodynamic Assessment and Calculation of Phase Diagram ", *Journal of Phase Equilibria*, 14(1), pp.22 (1993).

[3]   T. J. Anderson and, I. Ansara, "The Ga-In (Gallium-Indium) System", *J. Phase Equilibria*, 12(1), pp.64 (1991).

[4]   N. Saunders and A. P. Miodownik, "CALPHAD (Calculation of Phase Diagram): A Comprehensive Guide ", *Pergamon Materials Series*, Pergamon (1998).